Contract No:

This document was prepared in conjunction with work accomplished under Contract No. 89303321CEM000080 with the U.S. Department of Energy (DOE) Office of Environmental Management (EM).

Disclaimer:

Summary of Chloride-induced Stress Corrosion Cracking Experiments with a Spent Fuel Storage Canister Large Plate

Spent Fuel and Waste Disposition

Daniel Foley
Emmanuel E. Perez
Andrew J. Duncan
Lisa N. Ward
Thanh-Tam T. Truong
Robert L. Sindelar
Savannah River National Laboratory

Savannah River National Laboratory®
OPERATED BY SAVANNAH RIVER NUCLEAR SOLUTIONS

EXECUTIVE SUMMARY

This report provides a comprehensive summary of the crack growth rate testing and the experiments to evaluate the corrosion behavior of welded plate material taken from the Sandia National Laboratories' full-size mockup of a spent nuclear fuel (SNF) dry storage canister. The information includes that previously reported, and new work on detailed surface characterization of the corrosion attack from the large plate experiment. The work and the results inform aging management programs for the SNF canisters.

Crack Growth Rate Testing

Tests to determine crack growth rate were conducted using ASTM E1681 bolt-load compact tension specimens with an experimental setup designed to allow the initially dry salt deposits to deliquesce penetrate to the crack front under temperature and humidity conditions relevant to dry canister storage environments. Crack growth rate results were found to match existing experimental data from open literature compiled by SNL and EPRI. The compiled experimental data was gathered to develop a temperature dependent (K insensitive) crack growth rate model in support of flaw disposition in ASME Boiler and Pressure Vessel Section XI Code Case N-860 "Examination Requirements and Acceptance Standards for Spent Nuclear Fuel Storage and Transportation Containment Systems."

SRNL Large Plate Experiment

Knowledge of the salt, temperature, and humidity conditions for CISCC including the stress intensity factor, K_{ISCC}, were used to set up the "large plate" experiment. Seven through wall and part-through wall defects were manufactured via electrical discharge machining (EDM) in the weld residual stress field of the 51x46x1.6 cm section of the Sandia National Laboratories' full size mockup dry storage container with a circumferential weldment. Analysis of stress intensity factors for potential flaws in the residual stress fields of axial and circumferential weldments typical of a dry storage canister

A marine salt solution was prepared in accordance with ASTM D1141 "Standard Practice for Preparation of Substitute Ocean Water" and applied to the plate specimen with an airbrush in accordance with section 10.2 of ASTM G41 "Standard Practice for Determining Cracking Susceptibility of Metals Exposed under Stress to a Hot Salt Environment,". The plate was then allowed to dry before it being placed over a salt bed and exposed to a sustained 71-73% RH atmosphere at 22°C for a two-year experimental duration.

Visual examination of the plate during and after the 2-year exposure found that buildup of corrosion products was prevalent across the surface of the plate during the first days of exposure, however, few marked changes in appearance occurred after the first month. Upon removal from the exposure environment, an initial visual inspection of the plate was performed to measure surface corrosion coverage. Following the initial visual inspection the plate was cleaned and examined using a combination of non-destructive and destructive examination. Non-destructive

examination consisted of visual analysis, surface microscopy, penetrant testing, and ultrasonic testing. Destructive analysis was performed using serial sectioning parallel to the top surface of the plate on one EDM defect (VP-2).

Prior to cleaning, an initial visual analysis was performed on a selected area of the plate surface according to JIS G 0595 to gauge surface rust coverage. This analysis found that surface rust coverage rate somewhere between RN 2 (47% coverage) and RN 3 (32%) coverage. After cleaning a second visual analysis was performed using grid counting on the entire plate surface to gauge residual corrosion surface coverage. The results of grid counting found that 22% of the plate surface showed visual indicators of corrosion.

Surface microscopy was used to characterize corrosion pitting behavior within several areas of interest on the plate surface identified during post-cleaning visual examination. Corrosion pits outside of the weldment were found to be mostly spherical or elliptical in nature with some crevicing observed. Corrosion on the weldment was found to be predominantly crevicing or possibly filiform in nature. Corrosion pit densities for the areas of interest range from $1.19x10^6 - 3.87x10^7 \frac{pits}{m^2}$ with the average of the ten largest pits sizes for each region of interest ranging from $0.0773 - 0.2069 \ mm^2$. The maximum pit size identified in the areas of interest was $0.3135 \ mm^2$. Microscopic inspection for surface SCC in the areas of interest was unable to identify any cracks.

Destructive examination of the VP-2 EDM defect via serial cross sectioning revealed small pits (maximum of $300 \ \mu m$ deep) and small ($< 44 \ \mu m$) SCC cracks originating at the manufactured defect. There was no correlation between pitting and cracking; and there was no correlation between the (calculated) stress intensity and the incidence and size of the cracks. These cracks were not detected by any NDE test method as the very small size of the cracks were not amenable to NDE detection. The maximum CISCC crack growth rate of 22 µm/year is below the lower bound of the 95% confidence interval for crack growth from the SNL model.

The experiment metrics and the results are compiled in Table ES-1 below.

The termination of the plate experiment removed all salt. No additional exposure of the plate to cracking experiments is planned. The plate will be given to the University of South Carolina for use in patch development work and laser UT crack characterization under their NEUP project.
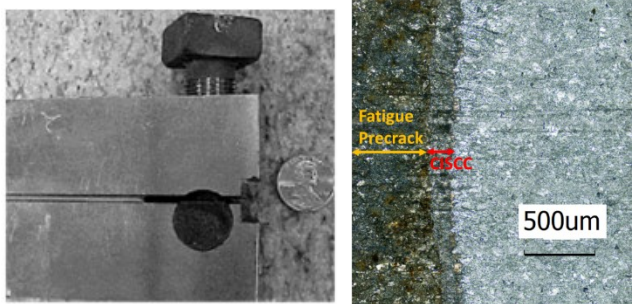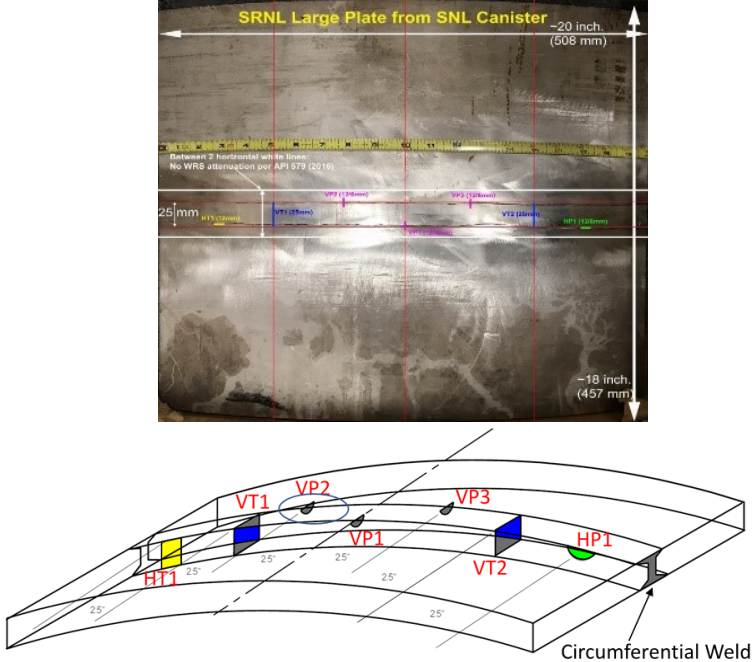
This report fulfills the M4 milestone M4SF-22SR010207082, "Characterization of Pitting and Cracking Behavior on the Mock-up Canister Plate" under Work Package Number SF-22SR01020708, Rev. 1.

Table ES-1 – Large Plate Experiment Results Summary

Experiment Metric	Notes	Thumbnail Picture
Bolt-load CT specimen		
Teardrop specimen		
Plate Test Specimen	Dual-certified 304/304L plate, approximately 51×46 cm with thickness 16 mm and weight about 30 kg containing a circumferential weldment. Seven (7) electrical discharge machined defects throughwall and part-throughwall, perpendicular and parallel to the weldment in the residual stress region of the weldment	
Applied Salt Loading onto Plate	2.3 g/cm^2 chloride using ASTM D1141 salt applied in spray and dried on plate prior to exposure to temperature and	Estimated Salt Load on Top Surface: 2.3 g/m2 chloride (Dry) (From artificial sea water prepared by ASTM D1141)

Experiment Metric	Notes	Thumbnail Picture
	humidity in an enclosed plexiglass chamber	
Test Start/Stop Dates	May 8, 2019 to May 12, 2021	
Additional Salt Loading onto pre-defect VP2 and HP1	Estimated < 5 g/cm^2 applied September 2019.	
Testing Temperature	22°C - Non-controlled ambient room temperature	
Testing Relative Humidity	71-73% - Controlled with ASTM E 104 salt system in box enclosure	
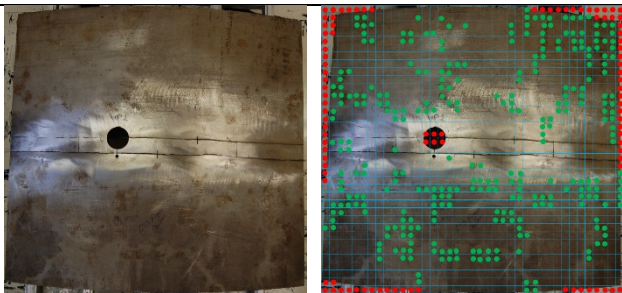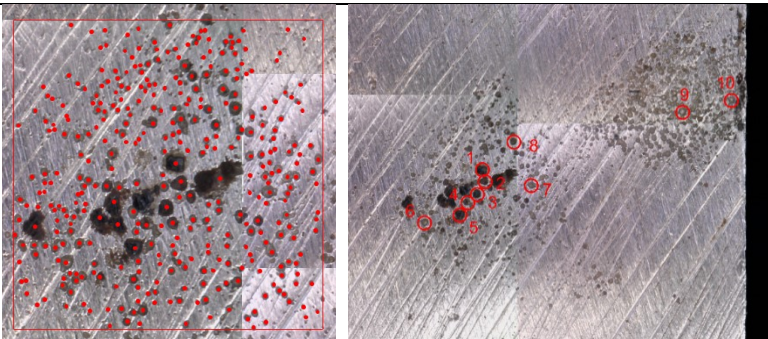
Experiment Metric	Notes	Thumbnail Picture
Initial Visual Test Results	Clear evidence of rusting and staining. The rusting appearance remained essentially unchanged after first month throughout the 2-year exposure period Examination via JIS G 0595 results in a rating between RN-2 and RN-3	

Experiment Metric	Notes	Thumbnail Picture
Post Cleaning Visual Test Results	Grid counting analysis of the cleaned plate resulted in 22% of the plate surface showing indicators of corrosion	
Penetrant Test Results	No evidence of SCC at weld toe region (crevice) or at surface out from 7 EDM defects	
Ultrasonic Test Results	Inconclusive with no definitive call of SCC from any of the 7 EDM defects	
Corrosion Pit Analysis Results	Corrosion pit densities in selected areas of interest ranged from 1.19×10^6-3.87×10^7. Cross sectional area analysis of the ten largest pits in each selected area of interest found average largest pit sizes ranging from $0.0773 - 0.2069 \ mm^2$. The larges measure pit size was $0.3135 \ mm^2$.	
Microscopic Analysis of Surface CISCC	No evidence of surface SCC could be identified in the region of interest.	

Experiment Metric	Notes	Thumbnail Picture
Destructive Examination Results	Destructive examination sectioned starter defects and imaged them from bottom surface of the slices. Cracking and Pitting grows out from inside surface of starter defects into the section thickness of the plate.	 Depth: 0.120" (3 mm) below the top surface. Optical Micrograph of Notch VP-2
Maximum Observed Crack Growth Rate	CGR = 0.022 mm/year (0.044 mm maximum SCC crack depth observed after 2-year exposure, and assuming no initiation time) The maximum pit depth observed was 300 μm from inside surface of EDM defect into the section thickness of the plate. The images are at 0.06" (1.5 mm) beneath the top surface of the plate.	 Depth: 0.06" (1.5 mm) below the top surface.

ACKNOWLEDGMENTS

This page is intentionally left blank

CONTENTS

LIST OF FIGURES

LIST OF TABLES

ACRONYMS

AMP	Aging Management Program
API	American Petroleum Institute
ASME	American Society of Mechanical Engineers
ASTM	American Society for Testing and Materials
BLCT	Bolt-load Compact Tension (specimen)
BM	Base metal
BPVC	Boiler and Pressure Vessel Code
CISCC	Chloride-Induced Stress Corrosion Cracking
CGR	Crack Growth Rate
COD	Crack opening displacement
CRIEPI	Central Research Institute of Electric Power Industry (Japan)
CT	Compact Tension Specimen
DAS	Data acquisition system
DOE	US Department of Energy
EDM	Electrical Discharge Machining
EIS	Electrochemical Impedance Spectroscopy
EPRI	Electric Power Research Institute
GW	Guided Wave
HAZ	Heat Affected Zone
ISFSI	Independent Spent Fuel Storage Installation
I-NERI	International Nuclear Energy Research Initiative
JIS	Japanese Industrial Standard
KU	Korea University
LWR	Light Water Reactor
NDE	Nondestructive Examination
NE	Nuclear Energy
NRC	Nuclear Regulatory Commission
PAUT	Phased Array Ultrasonic Test
PL	Pulsed Laser
PNNL	Pacific Northwest National Laboratory
PS	Proof Stress (Stress at 0.2% strain)

PT	Liquid Dye Penetrant Testing
PZT	Piezoelectric Transducer
RH	Relative Humidity
RN	Rating Number
SAW	Submerged arc welding
SCC	Stress Corrosion Cracking
SIF	Stress Intensity Factor
SLDV	Scanning Laser Doppler Vibrometer
SNF	Spent Nuclear Fuel
SNL	Sandia National Laboratories
SRNL	Savannah River National Laboratory
UT	Ultrasonic Test
VT	Visual Inspection
WRS	Welding Residual Stress
XRD	X-ray Diffraction

1. INTRODUCTION

Since the spent nuclear fuel (SNF) dry storage canisters currently in use at Independent Spent Fuel Storage Installations (ISFSIs) across the United States are not required to be stress relieved; stress corrosion cracking has been identified as a potential concern due to the possibility of through wall cracking leading to a breach in the confinement boundary provided by the canisters. This is especially true for canisters at ISFSIs near coastal regions where chloride bearing salt deposits may form on the external surfaces of the canister as the canister. If the local relative humidity at such a site is high enough, salt deposits on the surface of the canister may deliquesce to form an aggressive brine. With welding residual stress acting as the driving force, chloride induced stress corrosion cracking (CISCC) may take place in the weldment and/or the heat affected zone (HAZ).

This report provides a summary of the results of experiments discussed in previous reports issued in 2019 [1], 2020 [2] and 2021 [3] as well as analysis of surface corrosion pitting behavior examined via optical microscopy. The following paragraphs provide a brief description of the experiments performed during this work. Additional details on individual experiments are provided in the original reports as cited.

A large section, which contains a circumferential weld, was cut from a mockup canister at SNL [1]. Crack growth rate testing was performed on samples harvested from this plate using instrumented bolt-load CT specimens based on ASTM E1681 "Standard test method for Determining Threshold Stress Intensity Factor for Environment Assisted Cracking of Metallic Materials". These specimens were loaded into a dry salt cradle and exposed to a constant 75% RH at 37^oC for two months. Another set of crack growth specimens were fabricated from the plate according to ASTM E1820 "Standard Test Method for Measurement of Fracture Toughness" and tested via the methodology described under I-NERI/USA-ROK Project Number 2016-001-K: Flaw Stability and Stress Corrosion Cracking of Austenitic Stainless Steel Canisters for Long Term Storage and Transportation of LWR Used Fuel [4]. These specimens were submerged in a chloride solution at 5% salinity which was held in a chamber maintained at 50^oC and 95% RH during testing. 304 stainless steel teardrop coupons were also included as companion specimens in the instrumented bolt load CT test. The teardrop coupon was originally designed to simulate weld microstructures [5] [6] and was used in this study as an indicator for susceptibility to cracking and pitting.

The remaining section of the plate, approximately 51×46 cm with nominal thickness 16 mm and weight about 30 kg, was prepared for use in the "large plate" demonstration of CISCC. Through-wall and part-through-wall (surface) starter cracks, either parallel or perpendicular to the weld, were fabricated in the weldment area using electrical discharge machining (EDM). The stress intensity factor (K) for each machined starter crack under canister welding residual stress was estimated by the American Petroleum Institute (API) 579 procedure [7] [8] [9]. Dry salt was applied over these machined cracks (estimated 2.3 grams Cl^-/m^2) and natural deliquescence was allowed to take place at room temperature approximately 22 °C and 73% relative humidity (RH) [1] [10]. The large plate test was initiated May 8, 2019 and completed May 12, 2021 after 2 years exposure. The large plate was taken out of the exposure cell and cleaned for

nondestructive examination (NDE) to inspect for stress corrosion cracks that might have initiated and grown from the edges of the starter cracks. The NDE was followed by destructive examination (DE) by serial sectioning from the plate surface of the selected starter defect into thin slices to reveal potential crack growth and crack morphology. Finally, a microscopic examination of several areas of interest on the surface of the plate was performed to characterize corrosion pitting behavior and attempt to identify surface SCC.

Sections 2 and 3 are mostly summarized from reference 8 and reference 3 respectively to provide a complete record of the experiment in this report. Section 4 briefly covers a surface analysis by JIS G 0595 described in reference 3 before describing new analysis of corrosion pitting via microscopic examination following the techniques described in ASTM G46 "Standard Guide for Examination of Pitting and Corrosion".

2. CRACK GROWTH RATE TESTS

In fracture mechanics, any material system susceptible to SCC which is exposed to a sufficiently aggressive environment at a sufficient load will experience SCC. This response can be described in terms of stress intensity factors by $K_{applied} > K_{ISCC}$ where $K_{applied}$ is the applied stress intensity factor and K_{ISCC} is the threshold Mode I stress intensity factor for SCC of that material system in that environment. It is important to note that K_{ISCC} is considered a material property for a material held at certain environmental conditions, below which SCC will not occur. Appendix C Article C-8500 of the ASME BPVC Section XI (citation) provides a general expression for calculating the crack growth rate (CGR) based on $K_{applied}$ (here denoted as K_I) and K_{ISCC}:

$$\frac{da}{dt} = exp\left[-\frac{Q_g}{R_g}\left(\frac{1}{T_{abs}} - \frac{1}{T_{ref}}\right)\right]\phi(K_I - K_{ISCC})^{\eta} \tag{1}$$

In equation 1, Q_g is the thermal activation energy for SCC, R_g the universal gas constant, T_{abs} the absolute metal operating temperature, T_{ref} the absolute reference temperature, ϕ the CGR coefficient, and η the CGR exponent. By fitting CGR data acquired under CISCC conditions to equation 1 it is possible to develop prediction tools which can be used to establish flaw re-examination intervals should flaws be detected on a canister.

2.1 Instrumented Bolt-Load Compact Tension Specimen

Bolt-load compact tension specimens were fabricated from both archival 304 stainless steel plates and from plate sections harvested from the dual certified 304/304L stainless steel full-size mockup canister. The specimen design was based on that described in ASTM E1681 as shown in Figure 1.
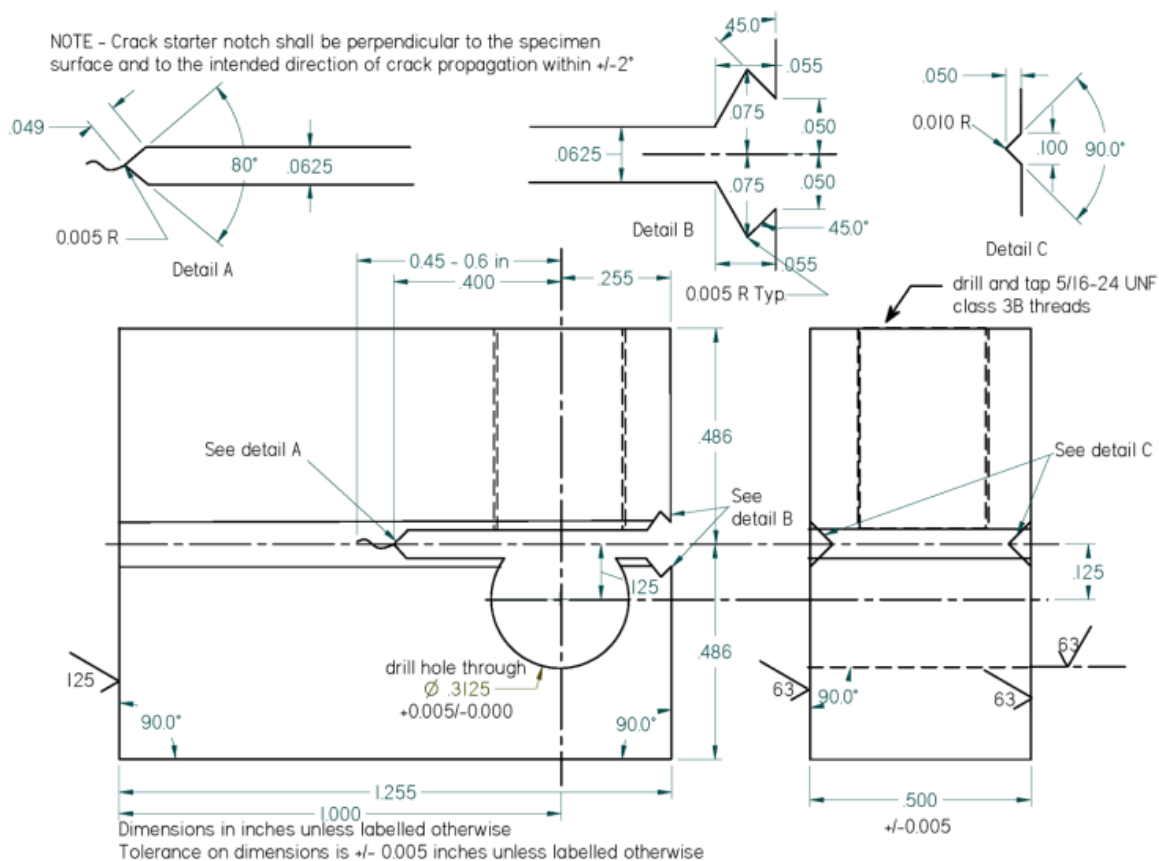
Figure 1: ASTM E1681 bolt loaded compact tension specimen design with 10% side groove on each side of specimen.

Pre-cracks were initiated by fatigue in air to produce a naturally sharp crack tip with an initial crack length between 12-15mm (or a/W= 0.5 to 0.6) as required by ASTM E1681. Stress intensity factors during fatigue cracking were kept as low as possible (~ 5-10 MPa√m) while maintaining consistent crack development in specimens within a 24 hour period. The pre-cracked specimens were cleaned with isopropyl alcohol and dried prior to being loaded to the desired stress intensity factors. Loading of the specimens was achieved by first elastically loading and unloading the specimen in an Instron 4507 mechanical testing machine while recording load and crack opening displacement (COD). Once the COD corresponding to the desired stress intensity factor was identified the specimens were then reloaded with an instrumented bolt to the desired COD. The stress intensity factor used in this experiment was calculated per equation 4 of ASTM E1681. The bolt-load CT test is conducted under "falling K" kinetics that would allow for the examination of the relationship between K and crack growth rate (da/dt), as well as providing data to determine a threshold value for stress corrosion cracking (K_{ISCC}), if it exists. Under this methodology as the crack grows, K drops until the CGR stops. This K level is referred to as K_{ISCC}. The CT specimens were loaded to approximately 33 MPa√m, the maximum possible per guidance in the standard to avoid plasticity effects. The instrumented bolt used in this study had

a built in load cell with a cable that passed through the feedthrough on both the glass vessel (environmental cell) and the oven to allow for load drop data acquisition during the course of the experiment.

2.2   Crack Growth Rate Test With Mixture Of Salt And Dust

Stress corrosion cracking may occur when chloride-bearing salts that may be present in a dust mixture deliquesce on the external surface of SNF canister in WRS regions. To simulate this scenario an experimental apparatus was designed to allow dried salt to deliquesce on the surface of the sample such that the brine will naturally infuse to the crack front of the instrumented bolt-load CT specimens under temperature and humidity conditions relevant to canister storage environments.

2.2.1   Experiment

The bolt-load CT specimens for this experiment were fabricated from a 12.7mm thick 304 stainless steel plate with 0.063 wt.% C archived prior to 1980. Three simulated dust and environmental conditions were examined as detailed in Table 1.

Table 1..Experimental conditions of exposure in dry salt crack growth testing

Test Cell Number Specimen Number	Environmental Conditions	Simulated Dust	
1	50 ºC and 50% RH[†]	98% CeO_2[‡] 0.8% NaCl 0.8% KCl 0.4% $CaCl_2$	
2	50 ºC and 50% RH[†]	50% Washed Sand[*] 12.5% Kaolin 12.5% Feldspar 25% Artificial Sea Salt[§]	(-200 mesh)[‡‡]
3	50 ºC and 30% RH[‡]	50% Washed Sand[*] 12.5% Kaolin 12.5% Feldspar 25% Artificial Sea Salt[§]	(-200 mesh)[‡‡]

* Secondary compounds of sea sand besides SiO_2 can be Zircon, Ilmenite and Rutile

† Achieved using ASTM E104 saturated aqueous solution of NaBr

‡ Achieved using ASTM E104 saturated aqueous solution of $MgCl_2$

§ Composition and form as specified by ASTM D1141

‡ SRNL legacy salt/dust mixture − CeO_2 particle size is not available (surrogate for PuO_2)

‡ By standard conversion, the particle size for 200 mesh is 0.074 mm.

A constant RH atmosphere was achieved using ASTM E104 "*Standard Practice for Maintaining Constant Relative Humidity by Means of Aqueous Solutions*" and the artificial sea salt was prepared in accordance with ASTM D1141, "*Standard Practice for the Preparation of Substitute Ocean Water.*" The salt/dust composition for Test Cell 1 is based on previous corrosion studies [5] [11] and is intended to be an artificially aggressive condition due to the high level of $CaCl_2$ while the compositions for Test Cells 2 and 3 were selected to be more relevant to canister service conditions. The dry salt assemblage was held to the specimen in the form of a cradle while both the specimen and the dried salt assemblage were suspended over an ASTM E104 humidity control solution inside a glass vessel which acted as an environmental chamber. A schematic configuration of the experiment setup is provided in Figure 2.

An Instrumented Bolt
Measures the Load Drop
With Crack Extension

Dry salt/dust mixture held around specimen surface perpendicular to crack plane

ASTM E104 Humidity Control Solution

Equilibrium Relative Humidity (ASTM E104):

Sodium Chloride
NaCl at 25 °C → 75 ± 0.6% RH

Sodium Bromide
NaBr at 50 °C → 50.9 ± 0.6% RH

Magnesium chloride
$MgCl_2$ at 50 °C → 30.5 ± 0.2% RH
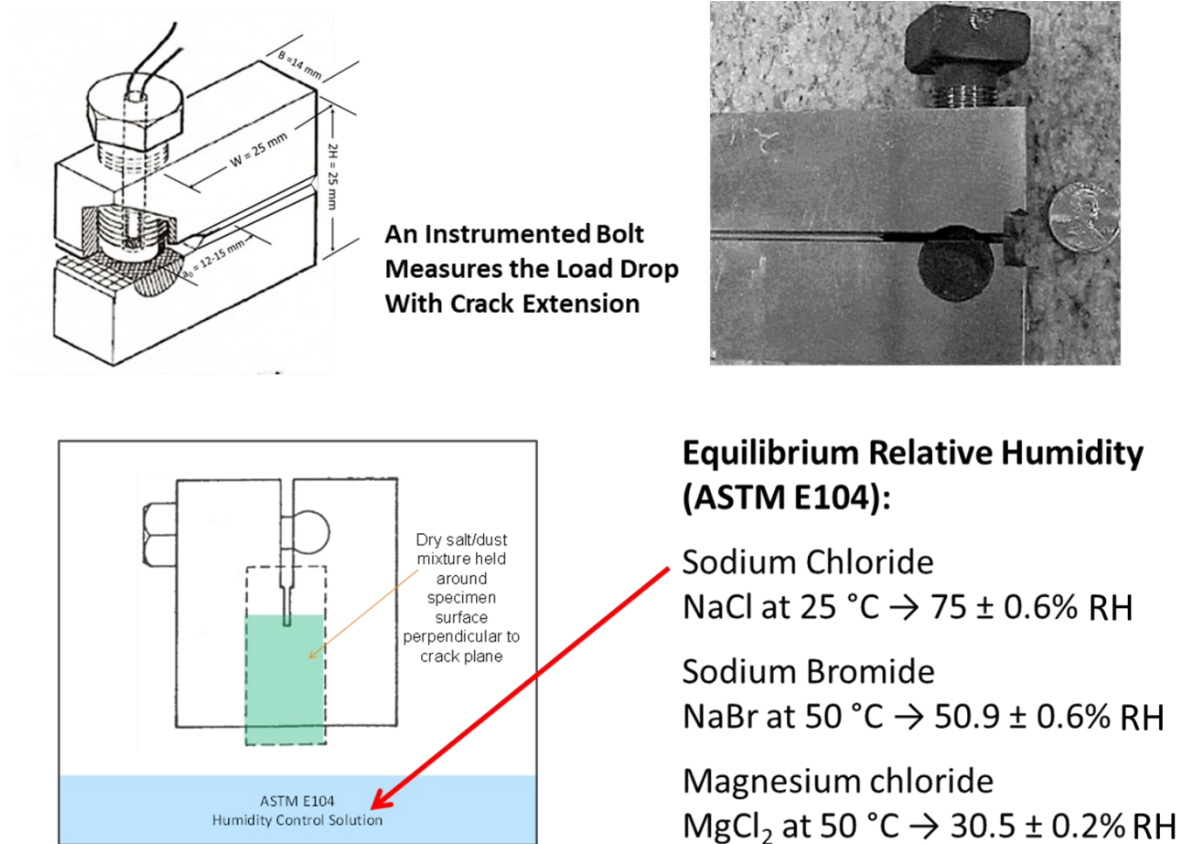
Figure 2: Typical arrangement of the bolt-load CT specimen in the constant humidity vessel.

To gather visual evidence of deliquescence and corrosion without unloading and removing the bolt-load CT specimens from the test environment a 304L stainless steel teardrop coupon was loaded into a glass cradle inside the environment chamber as a companion specimen. Dry salt was packed between the teardrop coupon and its cradle to ensure that crevice corrosion would not occur. An example of the complete loading arrangement is provided in Figure 3.
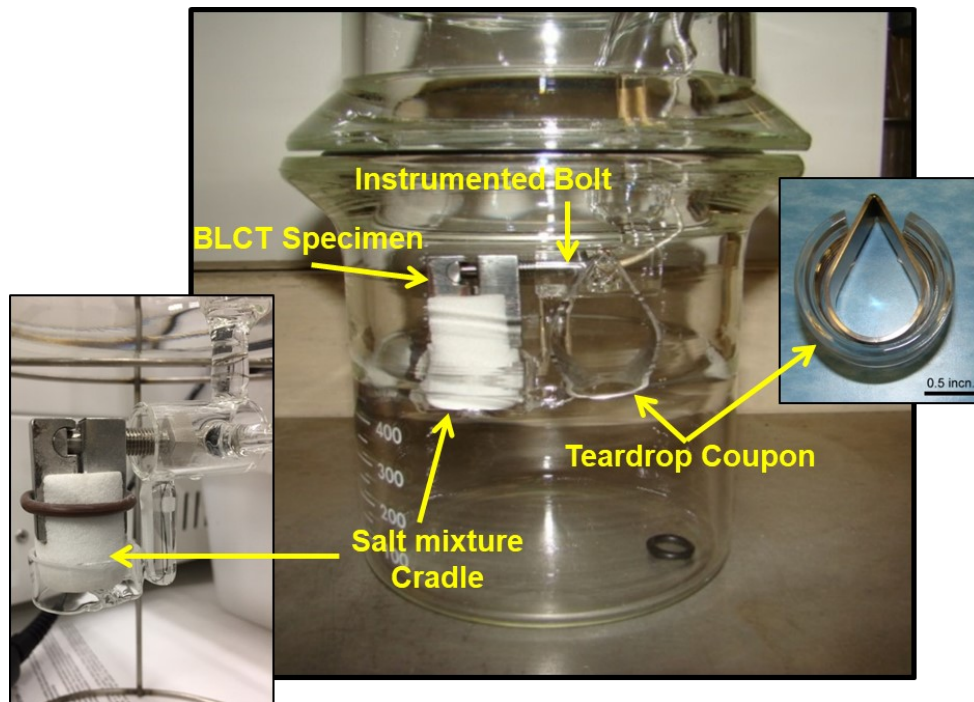
Figure 3: SCC test configuration showing the cradled instrumented bolt-load CT (BLCT) specimen and a companion teardrop coupon in a constant humidity vessel.

Once loaded the environmental chamber was placed inside an oven which was set to the desired testing temperature for 5 months before the specimens were unloaded for analysis.

2.2.2 Results

After 5 months of exposure the specimens were removed from the environmental chambers for examination. Figure 4 shows that both the bolt-load specimen and the teardrop coupon from Test Cell 1 exhibited corrosion around areas where the specimen was in contact with the dust/salt and even had dust/salt mixture clumped on their surface. The bolt-load CT and teardrop specimens from Test Cells 2 and 3 did not show any visible signs of corrosion and had a smaller amount of dust/salt adhered on their surface.

Examination of the bolt load CT specimen taken from Test Cell 1 reveals that at $50^{o}C$ and 50% RH, the simulated dried salt residue will deliquesce and induce pitting corrosion and cracking in 304 stainless steel as depicted in Figure 5. Unfortunately, the nature of the cracking in this region was not planar and therefore the associated stress intensity factor and CGR are difficult to characterize. In the cases of the artificial sea salt/dust mixtures in Test Cells 2 and 3, pitting corrosion and cracking were not present. This is likely due to the absence of a brine film in contact with the surface of the specimens, indicating that capillary action to draw brine onto the crack face is not certain.

Figure 4: Specimens as removed from test cells (Cell 1: calcium rich salt, Cell 2: sea salt)
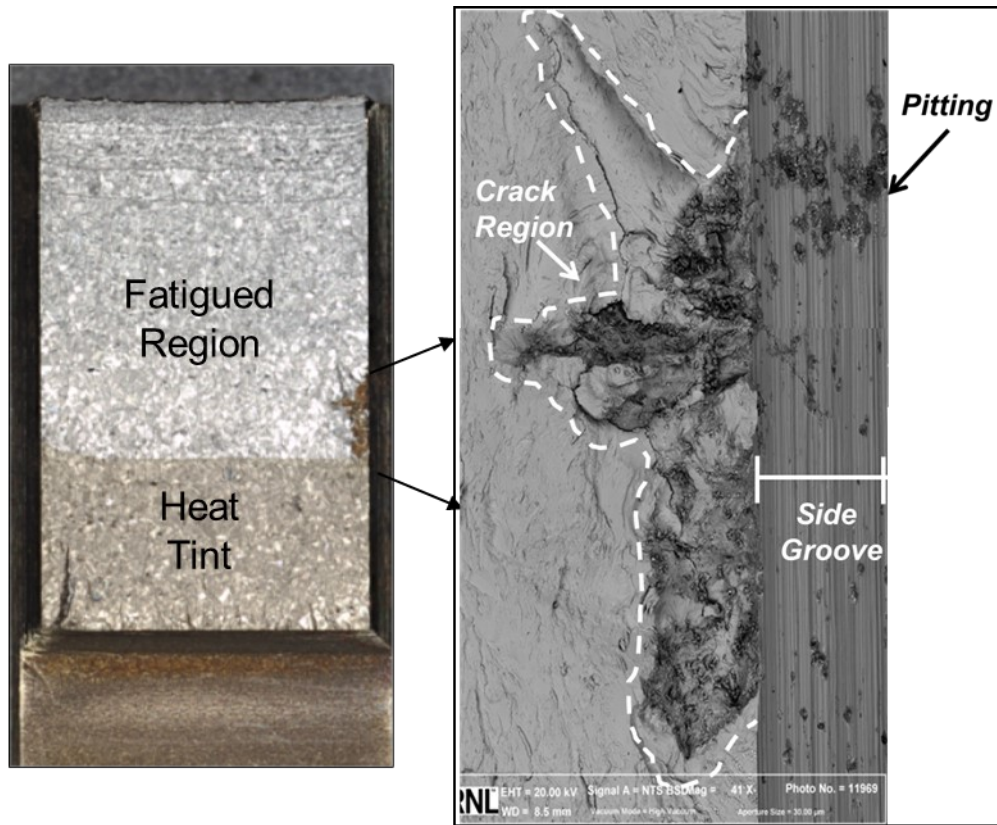
Figure 5: Optical and SEM images of the fracture surface of the bolt-load CT specimen (Specimen 1) exposed to simulated calcium-rich salt at 50 ºC and 50% RH for 5 months

2.3 Crack Growth Rate Test With Dry Salt

This section describes the CGR testing with instrumented bolt-load CT specimens harvested from the section of the mockup canister. Specimen geometries used are similar to those discussed in Section 2.1. Due to the geometry of the plate, a slight curvature was present in the specimens. The bolt-load CT specimens were packed with dry salt and tested under favorable environmental conditions to induce CISCC. CGR is calculated from the elapsed time average of the difference between the initial and final crack lengths.

2.3.1 Experiment

The samples used for this experiment were machined from two small plates cut from the SNL full sized mockup canister. One of the plates contains an axial (longitudinal) weld and the other has a circumferential (girth) weld. Figure 6 shows a schematic of the collection points for the two plates and depicts how the bolt-load CT specimens were machined from the plates.
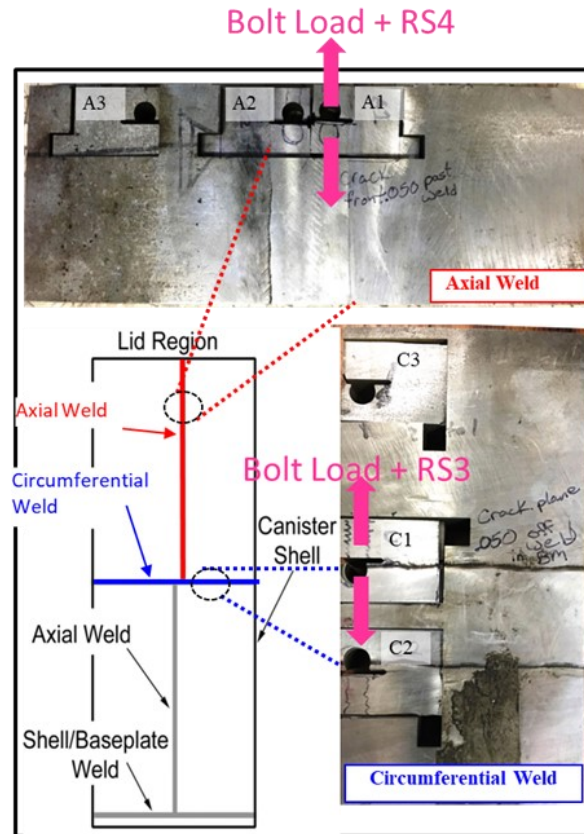
Figure 6: The Bolt-Load CT specimens as machined from two plates cut from the mockup canister

The design, pre-cracking, and loading procedure for the bolt-load CT specimens in this experiment mirror those discussed in Section 2.2.1. The dried salt assemblage for this experiment was limited to dehydrated, artificial sea water prepared according to ASTM D1141. A chemical-free cellulose wick was inserted at the end of the machined notch of the bolt-load CT specimen to assist with transportation of the deliquescent salt brine to the crack front. The desired 75% RH and temperature were achieved via ASTM E104 using an aqueous sodium chloride saturated salt solution in the bottom of the glass environmental vessel. Table contains a test matrix of the different bolt-load CT specimens depicted in Figure 6.

Table 2: Crack growth rate test matrix using bolt-load CT specimens

Sample	Sample ID	Temperature	RH	Thermal History	Orientation
Axial 1	A1	22°C (Room Temperature)	75%	HAZ	TL
Circ. 2	C2			HAZ	
Axial 3	A3			BM	
Axial 2	A2	37°C	75%	HAZ	TL
Circ. 1	C1			HAZ	
Circ. 3	C3			BM	

- Samples 1 & 2 cut from heat affected zone (HAZ)
- Sample 3 cut from Base Metal of plate (BM)
- Dehydrated Salt Residues (95°C for 72 hrs) from ASTM D1141 simulated sea salt

2.3.2 Results

The base metal bolt-load CT specimens, A3 and C3, (see Fig. 14 and Table 3) were removed from the test apparatus at the end of two months; while specimens A1, A2, C1, and C2, which are associated with the HAZ, remained in the test setup for six months. All specimens after testing were cleaned by following ASTM G1, "*Standard Practice for Preparing, Cleaning, and Evaluating Corrosion Test Specimens.*" Final crack lengths were established first by heat tinting the specimens at 350°C for 30 minutes to mark the final crack front, then break open the specimen in halves by fatigue. The crack lengths were measured with an optical microscope in compliance with ASTM E1681 at the transition from heat tint and un-oxidized fatigue surface. Figure 7 is a typical fractured surface (from Specimen C1 after exposure for six months). It shows the regions of fatigue pre-cracking, CISCC (Δa), and the final fracture by fatigue.
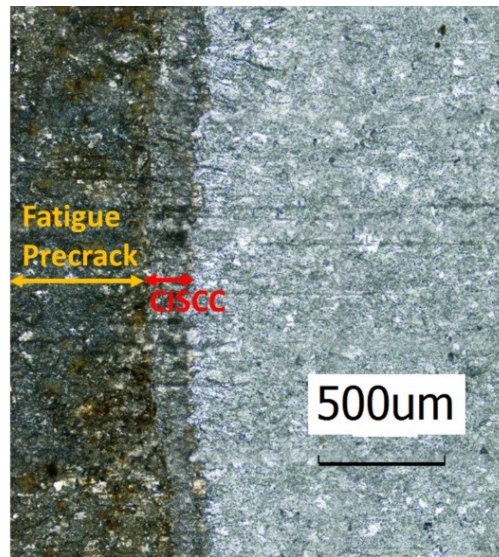
Figure 7: Typical fracture surface under CISCC from specimen C1

Table 3 summarizes the CISCC test results for all six bolt-load CT specimens up to six-month exposure. Examination of the results in Table 3 reveals that test temperature does not appear to have a significant effect on crack growth, which could be a result of these measurements being within experimental error. Regardless, the results do indicate that crack growth near the axial weld (Specimens A1 and A2) was faster than crack growth at the circumferential weld (Specimens C1 and C2).

Table 3: Results of bolt-load CT tests up to six months

304L Specimen	Actual Temp. (°C)	Actual RH (%)	Initial a/w	Final a/w	Initial K $(ksi\sqrt{in})$	$\Delta a\ (\mu m)$	GCR $(mm/year)$
C1 (HAZ)	37	74±3	0.60[b]	0.62[b]	30	137[b]	.274
C2 (HAZ)	24±2	74±3	0.50[c]	0.52[b]	32	230[b]	.460
C3 (BM) (2-month exp.)	37	74±3	0.78	0.78[b]	30	-	-
A1 (HAZ)	24±2	74±3	0.63[b]	0.65[b]	30	526[b]	1.052
A2 (HAZ)	37	74±3	0.60[ac]	0.62[b]	31	614[c]	1.228
A3 (BM) (2-month exp.)	24±2	74±3	0.61[b]	0.62[b]	30	188[b]	1.128

a: *Initial values measured from side groove crack growth measurements*
b: *Measured using optical average of cracks fronts from fracture surface*
c: *Estimated from specimen compliance*

2.4   Companion Teardrop Specimens

In the experiments discussed in Sections 2.2 and 2.3 teardrop coupons were included in the glass vessel as companion specimens to the bolt-load CT specimens. These teardrop coupons were intended to act as convenient indicators of susceptibility to cracking and pitting. After being removed from the testing vessel, each of these teardrop specimens was examined to determine the extent of corrosion. Only one teardrop coupon, exposed to high level of $CaCl_2$ (0.4%) at 50 °C and 50% RH for 5 months (Test Cell No. 1 in Table 1), exhibited signs of significant corrosion as shown in Figure 8.
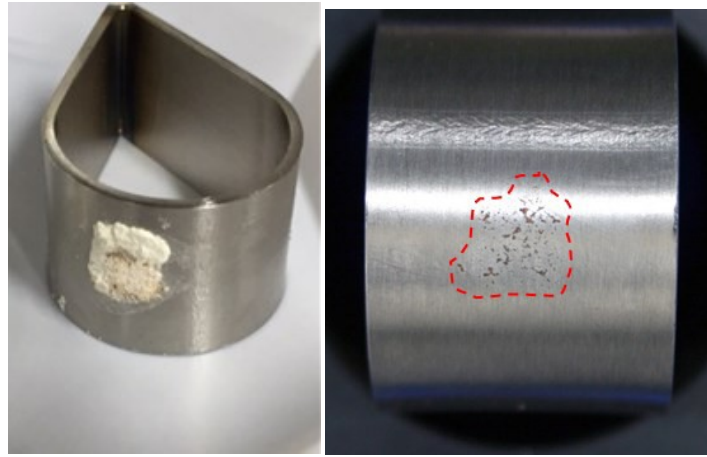
Figure 8: Adherent dust on teardrop Sample No. 1 following test (a) and the post cleaning image with outlined corrosion region (b)

The specimen was subjected to metallographic examination and analysis to further investigate pitting and cracking. First, the corroded region was imaged using laser confocal microscopy (LCM) to identify areas of interest. In particular, the LCM images of Area 1 and Area 2 in Figure 9 provided depth information for the corrosion pitting observed along lines A and B in Figure 10.
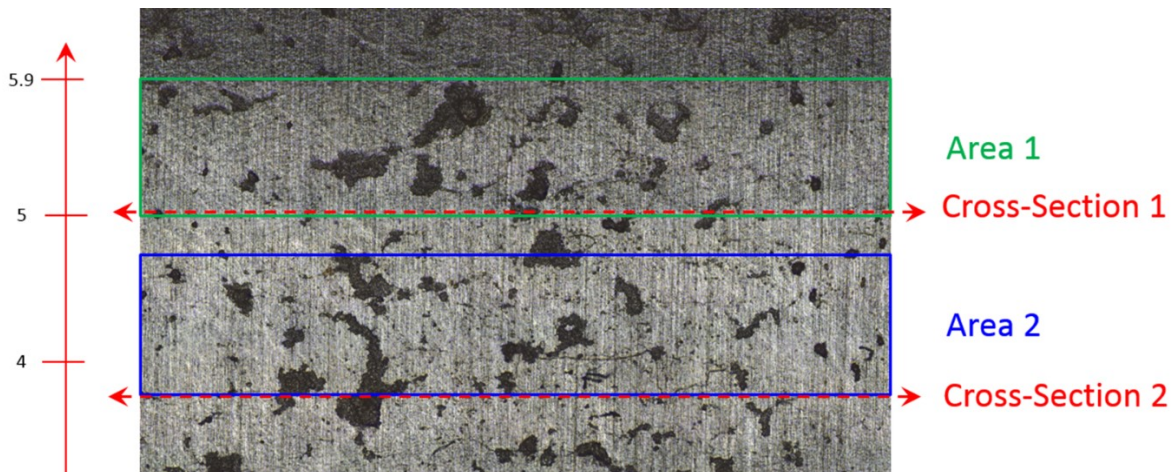
Figure 9: Image of the corrosion region on Sample 1
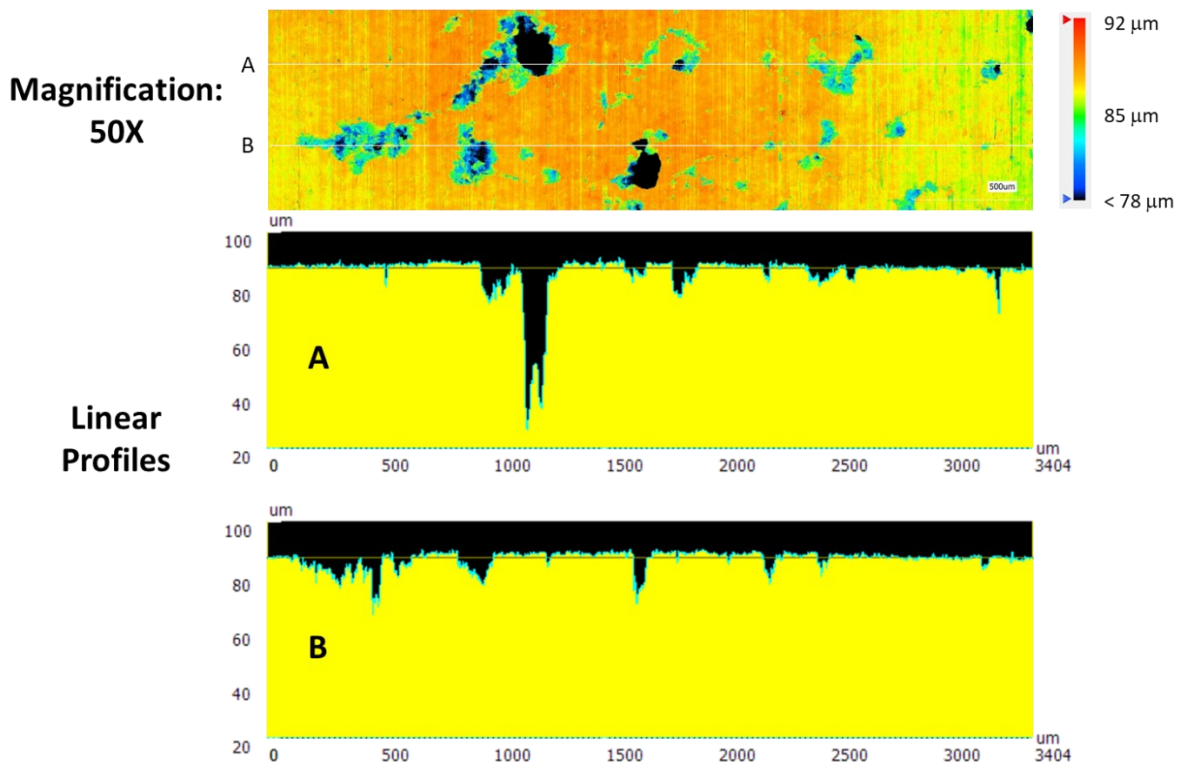
Figure 10: The LCM images of Area 1 in the corrosion area and the linear profiles of the cross-sections along Lines A and B, respectively

Cross-section B from Area 1 was mounted, polished, and electrolytically etched with oxalic acid (10%) and imaged at 50X magnification to observe cracking morphology. Images from the cross section, shown in Figure 11, indicate that cracking in primarily transgranular. The longest crack observed in Figure 11, depicted on the lower left of the image, was measured to be approximately $200 \mu m$ which corresponds to an average crack growth rate of 0.48 mm/year based on an exposure time of 5 months. Additionally, the cracks depicted in Figure 11 and Figure 12 demonstrate that cracks below the teardrop coupon surface are interconnected and the smallest pits (in terms of diameter and pit depth) appear to develop networks of "long" cracks.
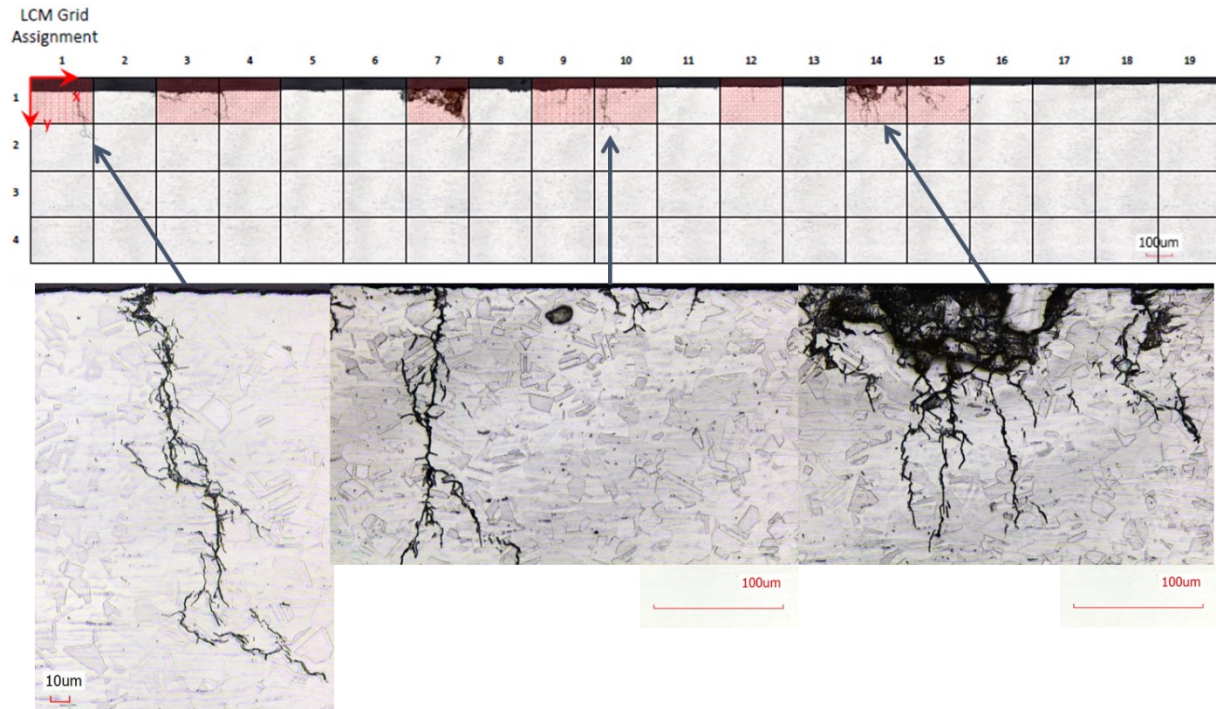
Figure 11: Images of cross-section B in Area 1 show transgranular stress corrosion cracks and pitting corrosion
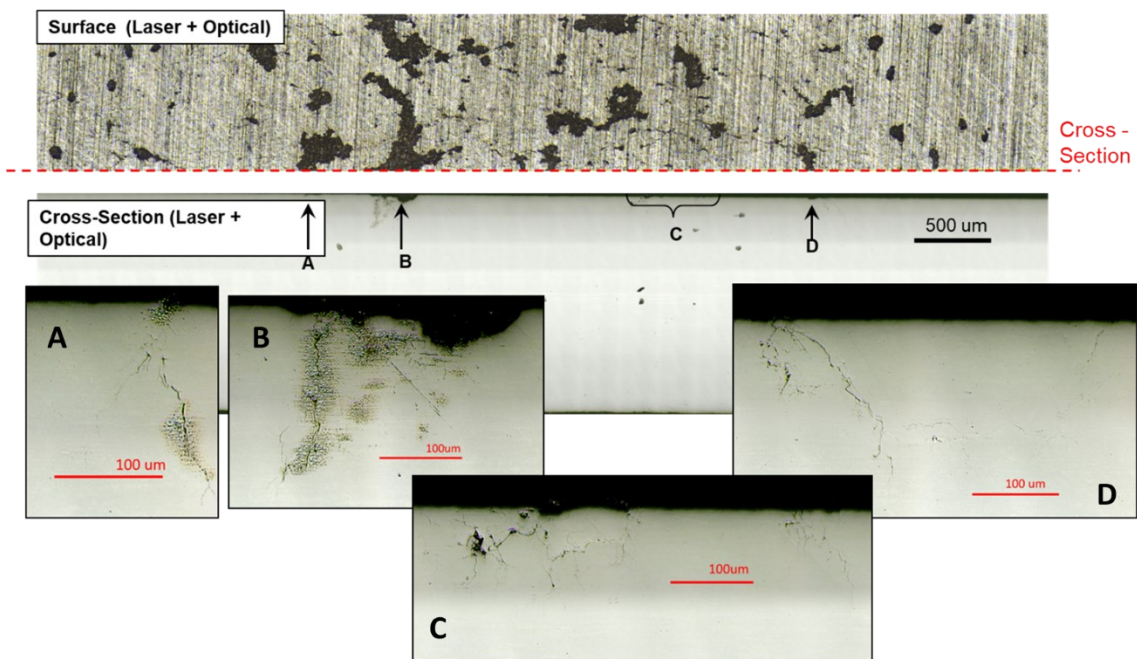
Figure 12: Images of the cross-section in Area 2 show transgranular stress corrosion cracks and pitting corrosion

Additional characterization of regions A, B, C, and D in the cross-section of Area 2 (Figure 12) were conducted. The pit depths and the associate SCC depth (lengths) were measured and indicated in Figure 13.
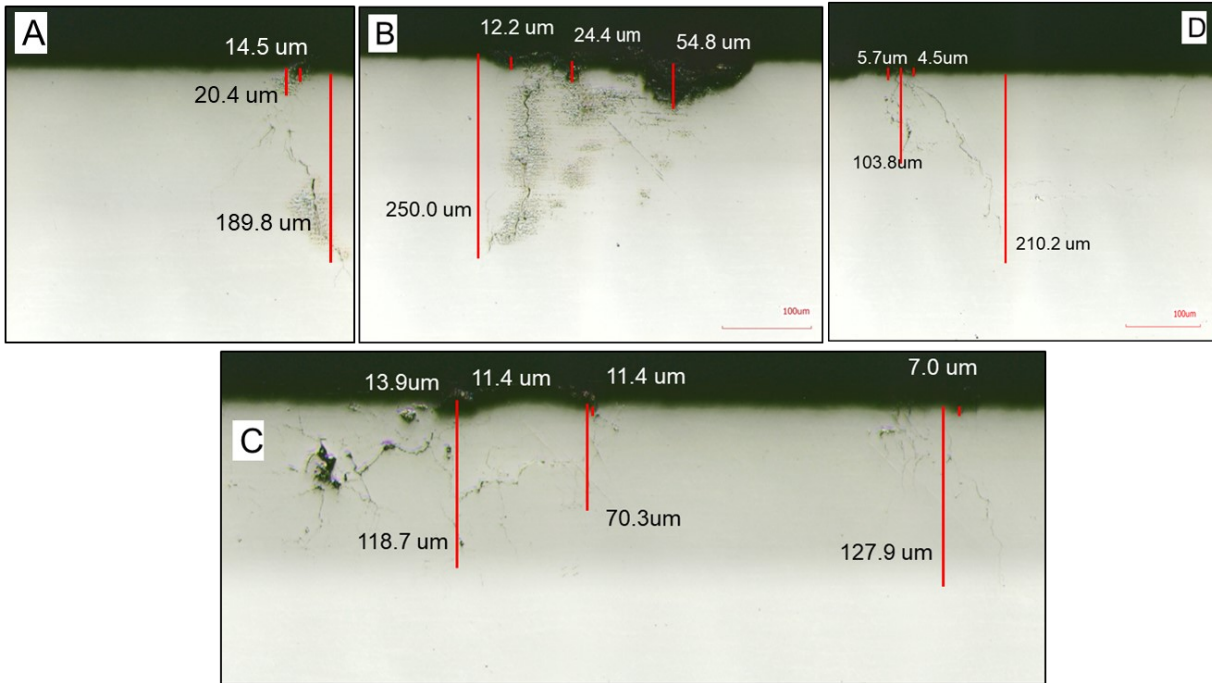
Figure 13: Characterization of pits and the associated stress corrosion cracks in sectioned teardrop coupon Sample 1

Plotting the results of crack length compared to pit depth reveals that there is no observable relationship between the two.
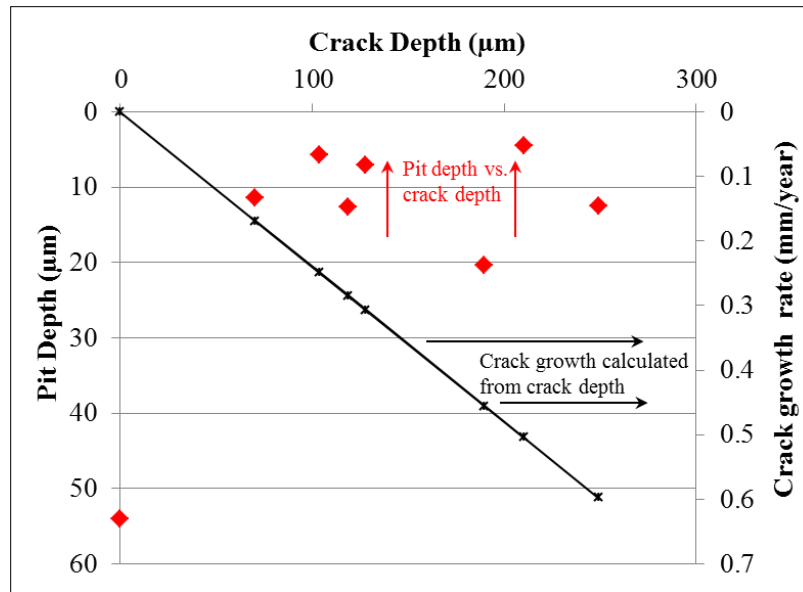
Figure 14: Relationship between pit depth and the associated crack depth (symbol ♦) as well as the corresponding crack growth rate (symbol ×) as converted from crack depth averaged by test duration (5 months)

Since no corrosion was observed on the teardrop coupons associated with Test Cells 2 and 3 a set of follow up tests was conducted on teardrop coupons with sea salt at 50ºC and 50% RH for 3 months. The results of these follow up tests indicate that an aggressive environment was achieved and cracking did occur during the 3 month test. Figure 15 shows results from these tests and illustrate the presence of CISCC in the teardrop coupons. Specimens are shown in Figure 15 (a), (b), and (c) for 100% sea salt, 25% sea salt/75% CeO_2, and 25% sea salt/75% artificial dust conditions, respectively. Once again a strong correlation between pit size and crack length could not be established.
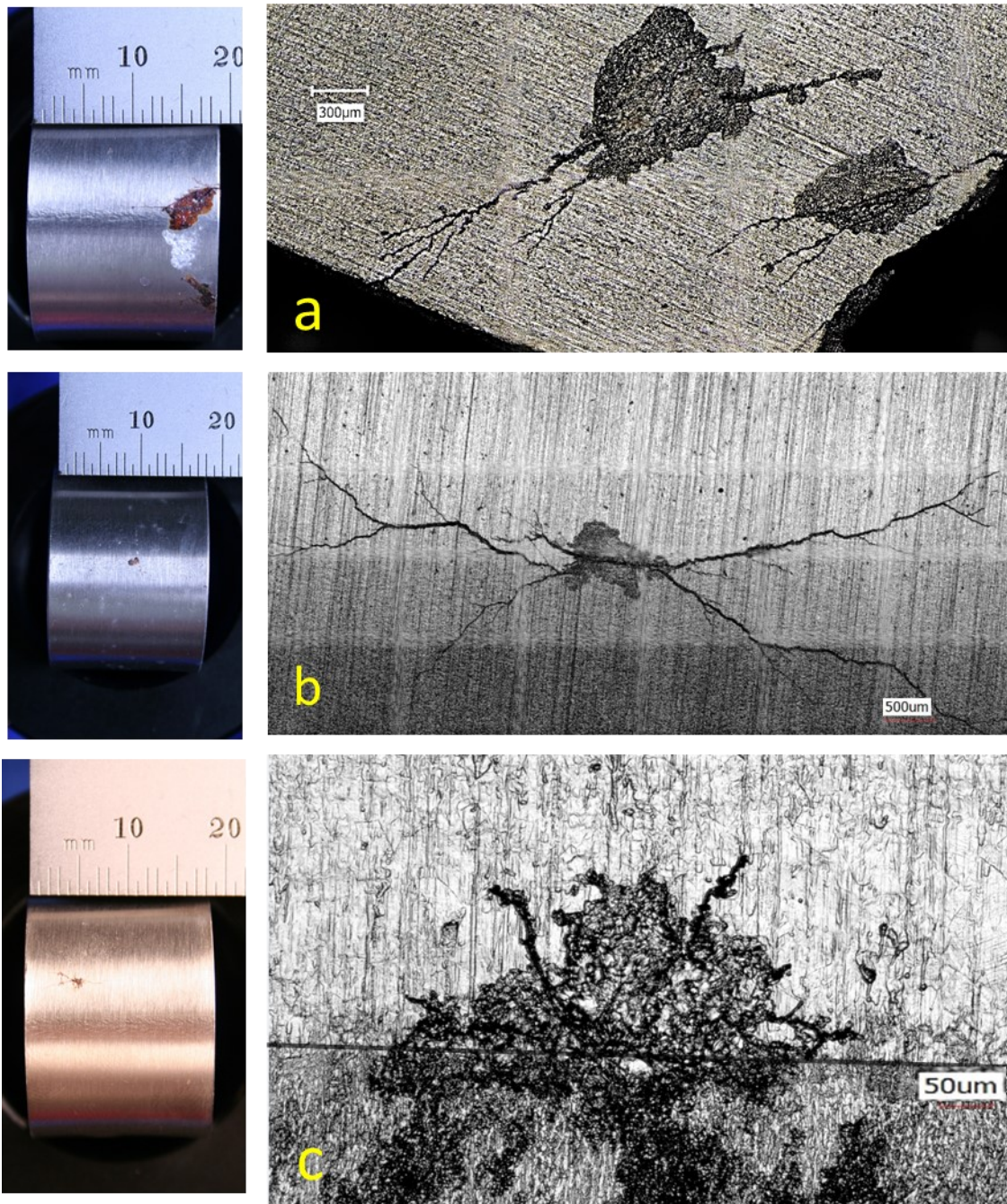
Figure 15: LCM images of cracking initiated on the surface of teardrop coupons at 50 ºC and 50% RH for 100% sea salt (a), 25% sea salt + 75% CeO2 (b), and at autogenous weld interface (shown by a dark line) in 25% sea salt + 75% artificial dust (c)

3. SRNL LARGE PLATE EXPERIMENT

Where the previous efforts described in this report were intended to gather data on the threshold stress intensity factor, the large plate demonstration conducted at SRNL is intended to demonstrate corrosion and cracking behavior at the structural level. The large plate used here consisted of a 51x46x1.6 cm section cut from the same full sized mockup canister as the bolt-load CT specimens described in Section 2 which contained a circumferential weld (Figure 16 provides a diagram of where the plate was cut from). The size of the plate was carefully determined from finite element calculations to minimize redistribution or relieving of WRS during cutting of the plate.
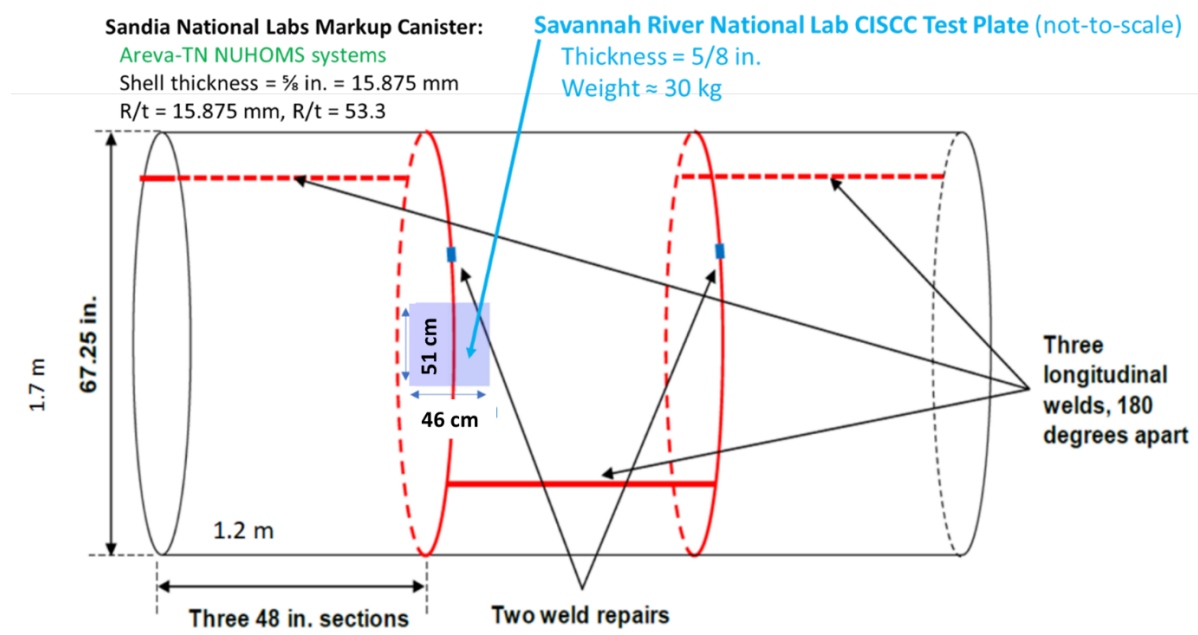
Figure 16: A sketch of the full size mockup canister showing the fabrication welds and the representative location where the SRNL large plate was harvested.

Avoiding redistribution or relief of WRS is critical for this analysis since WRS could become the mechanical driving force for SCC in corrosive environments. In a separate study at Oak Ridge National laboratory [12], neutron diffraction was used to determine the remaining WRS in their large plate also from the same mockup canister but with an axial weld. Their experimental data confirmed that most of the as-welded residual stresses were retained in the sectioned plate. Therefore, it is reasonable to assume that the residual stresses in the SRNL large plate were not altered significantly during cutting.

3.1.   Starter Cracks or Defects

Starter cracks or defects, also known as seed cracks, were introduced at several points along the weld region by EDM. These starter cracks are intended to create a favorable fracture

environments for stress corrosion cracks to initiate and grow under WRS loading. Seven starter cracks in total were machined into the plate and given the following designations:

Type (a) VT1, VT2: through-wall crack across the weld, crack length = 25 mm;

Type (b) HT1: through-wall crack parallel to the weld edge, crack length = 12 mm;

Type (c) VP1, VP2, VP3: semicircular part-through-wall crack (surface crack) perpendicular to the weld edge, crack length= 12 mm and crack depth = 6 mm;

Type (d) HP1: semicircular part-through-wall crack (surface crack) parallel to the weld edge, crack length= 12 mm and crack depth = 6 mm.

The orientation and layout of each crack is schematically shown in Figure 17 while the EDM crack configurations are shown in Figure 18.
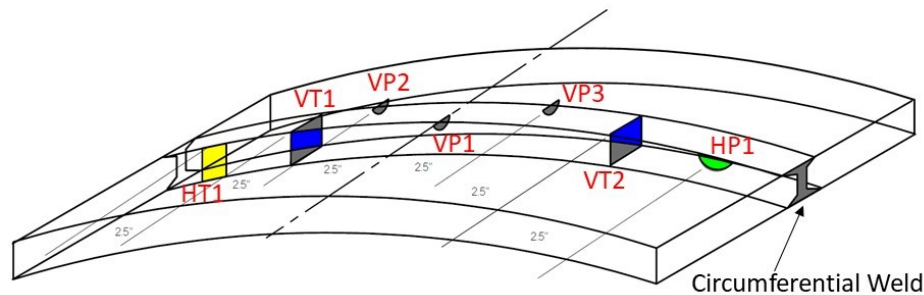
Starter Crack Description (total 7 EDM cracks):
VT1, VT2: Through-wall crack across the weld.
          Crack length= **25 mm**
HT1: Through-wall crack parallel to the weld edge.
          Crack length= **12 mm**.
VP1, VP2, VP3: Semi-circular Part-through-wall crack perpendicular to the weld edge.
          Crack length= **12 mm** and crack depth = **6 mm**
HP1: Semi-circular Part-through-wall crack parallel to the weld edge.
          Crack length= **12 mm** and crack depth = **6 mm**

Figure 17: Starter crack layout and orientation in the large plate.
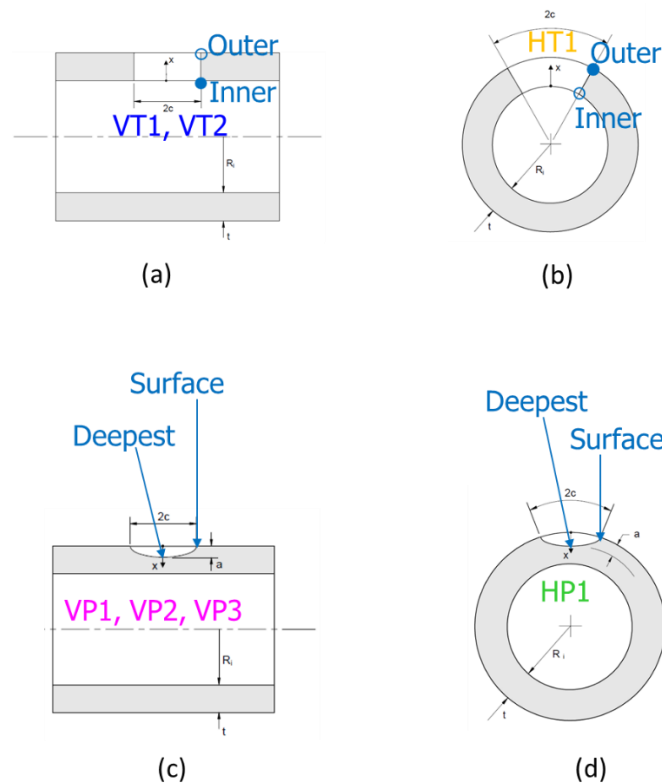
Figure 18: Large plate starter crack configurations: Type (a) VT1, VT2: through-wall crack across the weld; Type (b) HT1: through-wall crack parallel to the weld edge; Type (c) VP1, VP2, VP3: semicircular (a = c) part-through-wall crack perpendicular to the weld edge; and Type (d) HP1: semi- circular (*a* = *c*) part-through-wall crack parallel to the weld edge

When the starter cracks are overlaid over the contour map of residual stress parallel to the circumferential weld [13], the WRS loading of the cracks can be seen as shown in Figure 19
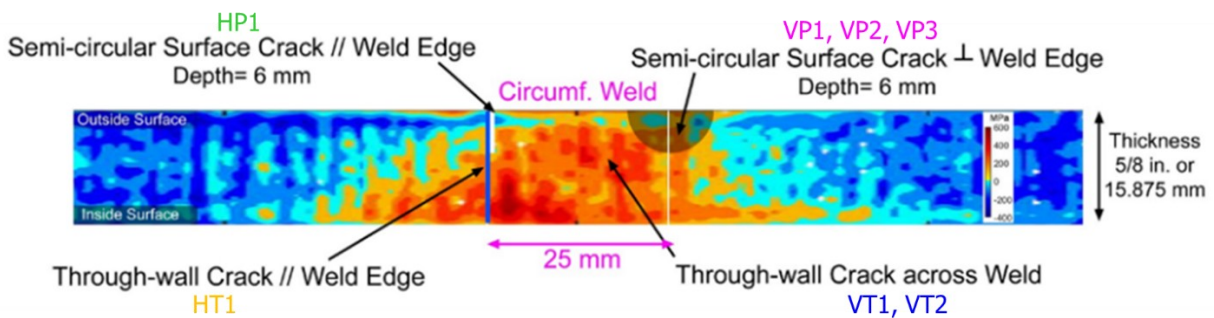
Figure 19: Large plate starter crack design as viewed from plate cross-section through the circumferential weld (superimposed over the contour map for welding residual stress parallel to the weld [13])

3.2.   Experiment

Artificial sea salt was prepared in accordance ASTM D1141 then deposited on the outer surface of the plate at a salt load of 2.3 g/m^2 chloride using an airbrush. This salt coating procedure is outlined in ASTM G41 "Standard Practice for Determining Cracking Susceptibility of Metals Exposed under Stress to a Hot Salt Environment," and is intended to achieve an evenly distributed salt layer on the plate surface. Once coated the plate was placed on risers over a salt bed inside a watertight 56 x 53 x 15cm Lexan box with 12.7mm wall thickness. The interior of the box was maintained 73% RH at room temperature in accordance with ASTM E104, "*Standard Practice for Maintaining Constant Relative Humidity by Means of Aqueous Solutions*". The box was opened on six month intervals to check the plate surface and apply additional salt loadings. Total exposure time was 2 years.

3.3.   Experimental Observations

The test was initiated on May 8, 2019. The temperature and RH reached equilibrium within one day. The initially dry salt film originally covered the plate surface turned into numerous liquid droplets in a few hours. This indicated that the natural deliquescence has taken place.

During the first five months of exposure periodical examination of the plate was performed and imaging of the seven starter cracks was acquired (see Figure 20).
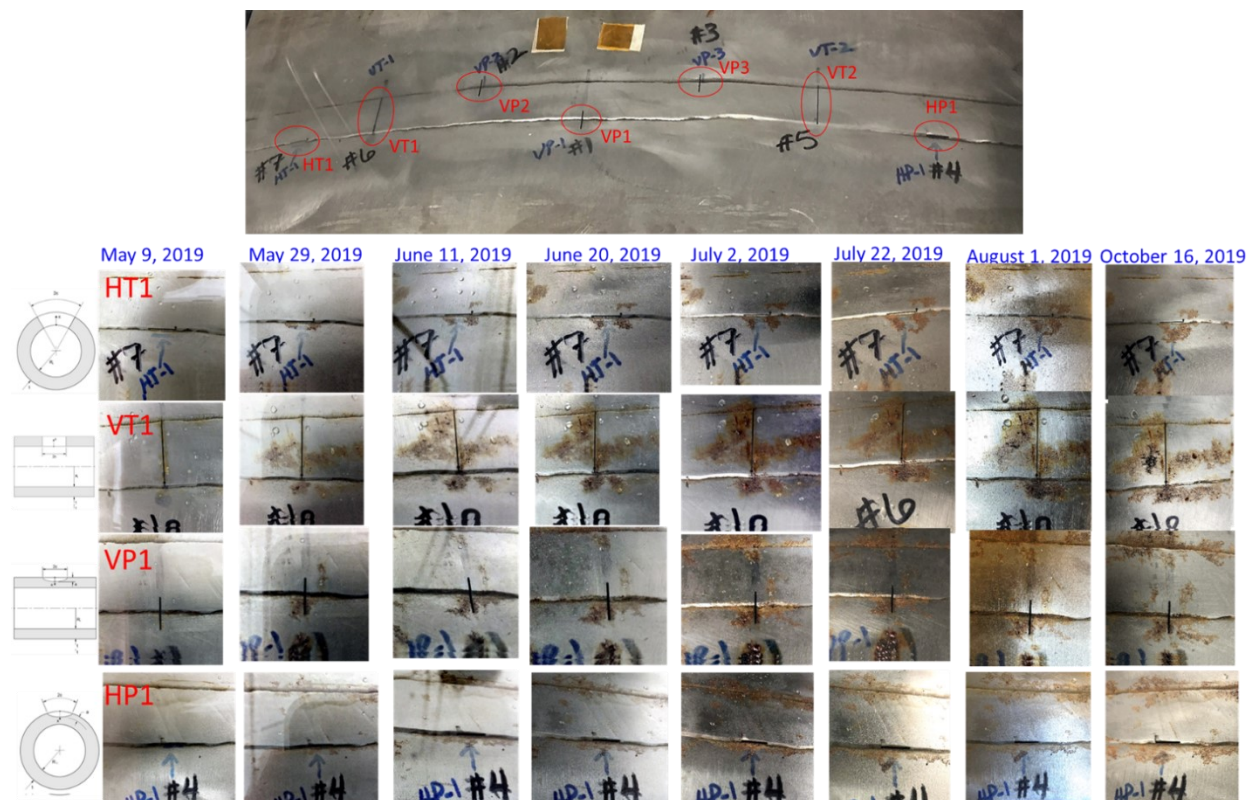
Figure 20: Evolution of chloride-induced corrosion near starter cracks during 5 months of exposure at room temperature about 22C and 73% RH

General corrosion was observed to progressively develop on the surface of the plate and especially along the weld to base metal interface. However, no cracking was observed at any of the starter cracks during this period.

Since cracking was not observed during the first five months of the experiment an additional salt load was added to two of the starter cracks (VP2 and HP1) to create a more a more aggressive corrosion environment. To achieve this, dry salt was placed on the regions surrounding the selected cracks. To prevent the water droplets that formed from the additional salt load from running off the surface of the plate a ring of plumbers putty was placed around the cracks as shown in Figure 21.

Figure 21: Additional salt applied to selected starter cracks (VP2 and HP1).

A comparison of general corrosion in the weld region between May 9, 2019 and February 21, 2020 found that the corrosion pattern appears to quickly stabilize. Even the areas with extra applied salt loading show little difference in general corrosion accumulation during this time period. Figure 22 shows images depicting the corrosion buildup on the plate from May 9, 2019 to February 21, 2020

Figure 22: Evolution of general corrosion on the large plate in weld region

3.3.1. Stress Intensity Factor Calculation Results

Since no external loads were applied to the plate during this test, and the weld present in the plate was circumferential on the full size mockup canister, only the WRS parallel to the weld will be relevant to SCC. The API 579 fitness for service procedure was used to calculate the stress intensity factor K_I for each of the starter cracks. A summary of the results are provided in Table 4. Note that several sets of the starter cracks (VT1/VT2 and VP1/VP2/VP3) have been grouped together in these results. This is because their starter crack descriptions, and by extension their WRS state, are effectively identical.

Table 4: Stress intensity factors for start cracks

Crack Identification	Welding Residual Stress	Crack tip Location	Stress Intensity Factor (MPa√m)
VT1 and VT2	Weld Centerline	Outside surface	51.6
		Inside surface	64.3
	Heat affected zone	Outside Surface	46.1
		Inside Surface	33.3
VP1, VP2, and VP3	Weld Centerline	Deepest point	26.0
		Surface point	16.9
	Heat affected zone	Deepest point	18.3
		Surface point	26.4
HP1	Weld Centerline	Deepest Point	5.6
		Surface Point	-3 (crack tip closure)
	Heat affected zone	Deepest Point	7
		Surface Point	12
HT1	Weld Centerline	Outside Surface	6.5
		Inside Surface	6.7
	Heat affected zone	Outside Surface	13.3
		Inside Surface	1.9

Examination of the starter cracks did not reveal signs of stress corrosion cracking.

3.4.   NON-DESTRUCTIVE EXAMINATION

After the large plate was removed from the environmental chamber it was visually inspected, photographed and then cleaned using a non-metallic wire brush and isopropyl alcohol. Liquid dye penetrant testing, and ultrasonic testing were performed to see if any evidence of SCC was present on the outside surface of the plate. The dye penetrant test did not find any indications of cracking, however, the ultrasonic shearwave test did pick an indication of potential flaw extension in the vicinity of starter crack VP2.

3.5.   Destructive Examination

After the NDE results were observed, a circular plug containing starter crack VP2 was sectioned from the large plate by EDM for metallographic analysis. Serial sectioning was performed by EDM to create thin slices at regular intervals along the depth of the flaw. Figure 23 contains a schematic of the sectioning performed and Table 5 provides information about the position of each sample relative to the top surface of the plate.
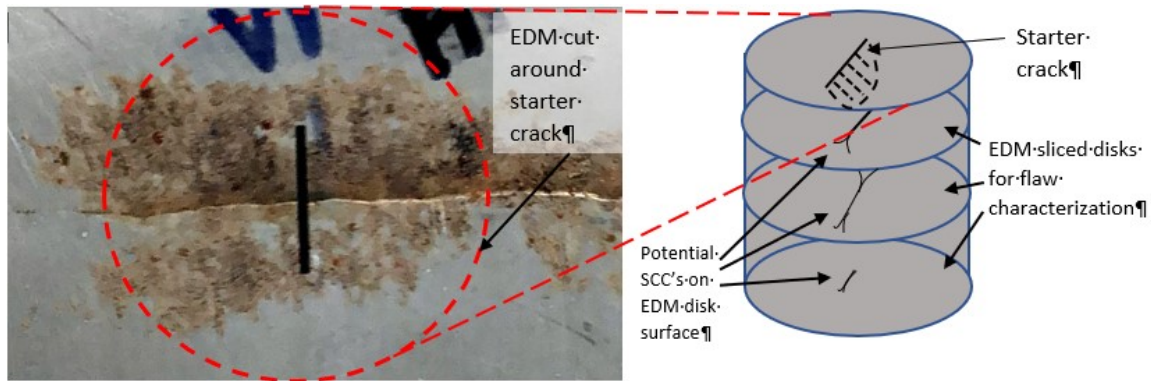
Figure 23: Schematic of serial sectioning of materials containing a starter crack along the depth of the stress corrosion crack.

Table 5: The position (depth) of each sample relative to the outside surface of the canister plate

Sample #	Top Depth (inches)	Bottom Depth (inches)	Thickness (inches)	EDM length at top/bottom of sample disk (inches)
1	0	0.06	0.06	0.472/0.4569
2	0.075	0.127	0.052	0.4480/0.3983
3	0.142	0.195	0.053	0.3775/0.2666
4	0.210	0.266	0.056	0.2162/0.0
5	0.281	0.338	0.057	
6	0.353	0.418	0.065	
remainder	0.433	0.683	0.25	

The sample slices were mounted to metallographic mounting epoxy with the bottom of the specimen facing up and polished for imaging. Secondary electron micrographs were taken on areas labelled 1-28 surrounding the starter crack as depicted in Figure 23. Multiple cracks and pits were observed on the inside surface of the starter crack as shown in Figure 24 images a-f.
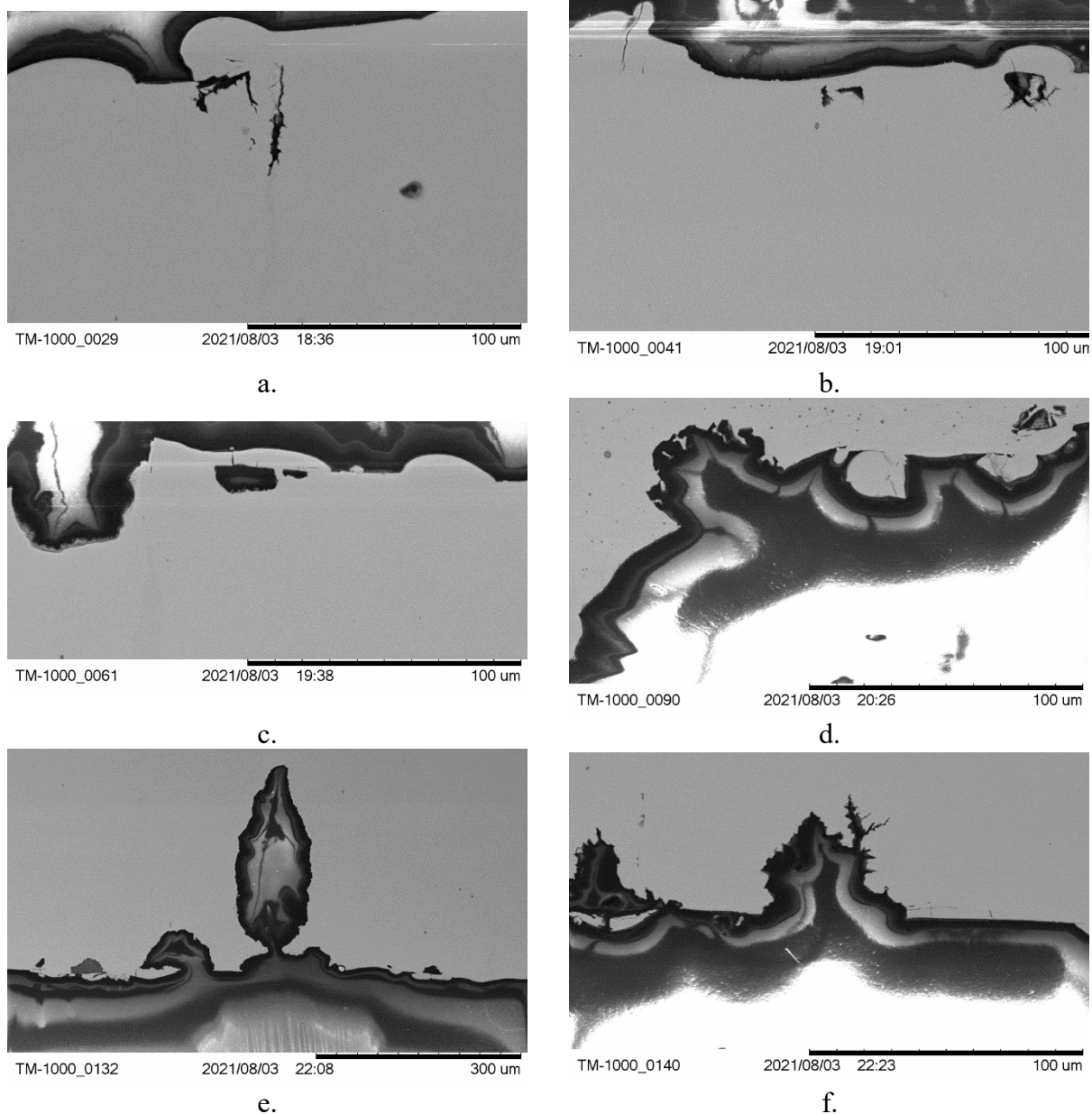
Figure 24: Secondary electron micrographs of pits and cracks from a. Sample 1, Area 1 b. Sample 1, Area 10 c. Sample 1, Area 5 d. Sample 1, Area 16 e. Sample 1, Area 26 f. Sample 1, Area 28

Crack lengths ranged from 5 to 45μm and pits up to 300μm deep were measured suggesting a time average CGR of approximately 23μm per year.

4. MICROSCOPIC SURFACE CORROSION ANALYSIS

One of the motivating factors for this experiment was to provide guidance for in-service inspection of SNF storage and transportation canisters. Currently, ASME Section XI Code Case

N-860 [14] provides in-service inspection requirements for examination of the accessible exterior metallic portions of the welded austenitic stainless steel SNF storage and transportation canisters. In Code Case N-860 Paragraph 2320 "Classification of Degradation," the visual anomaly shall be classified by degradation condition and location. The Japanese Industrial Standard, JIS G 0595, "Rating Method of Rust and Stain of Atmospheric Corrosion for Stainless Steels," [15] is used as an example to distinguish the severity between "major," "minor," or "insignificant" degradation.

Since JIS G 0595 is directly suggested in ASME Section XI Code Case N-860, it was applied to the large plate using a photograph (taken on a Nikon D-40 digital camera) taken of the plate prior to cleaning it. As described in reference [3] a strict application of the 100x150mm sampling size required for JIS G 0595 was not practical so a smaller 30x50mm sampling size, placed around starter crack VP2, was used instead. Estimation of rust coverage in the sample region was achieved by limiting the image to just the 30x50mm sample region, masking the un-corroded areas and then dividing the number of unmasked pixels by the total number of pixels. Based on this analysis, the rust coverages has a JIS G 0595 designation between RN 2 (47% coverage) and RN 3 (32% coverage). This rating would put the plate in the category of "major" surface corrosion according to ASME Section XI Code Case N-860 and may require additional actions. Yet, despite this rating no surface cracking was observed through the 2 years of exposure. Therefore it can be concluded that JIS G 0595 analysis alone is not sufficient to correlate CISCC to the surface condition

Since the JIS G 0595 proved to be insufficient to correlate CISCC to surface condition, complimentary analysis techniques which can be deployed in the field should be considered. One route would be to utilize handheld, portable microscope to examine the extent and size of surface pitting as well as search for cracks in areas of concern in a procedure similar to that described by ASTM G46 "*Standard Guide for Examination and Evaluation of Pitting Corrosion*".

4.1. Experiment

Prior to imaging and microscopic analysis the plate was cleaned of corrosion products with a non-metallic wire brush as described in Section 3. An initial image of the entire plate was acquired using a Nikon D-40 camera held over the plate at 1x zoom. A Dino-Lite Edge 5MP series digital microscope model number AM7115MZTW mounted on a Dino-Lite MS62W1 wheel-rack stand was used to take micrographs along the surface of the plate within a region of interest. Prior to collecting micrographs a metal guide was placed on the surface of the plate such that that the longitudinal edge of the guide was parallel to the edge of the plate. A ruler was used to establish the initial spacing of the guide so that the edge of the plate is initially at the outer edge of the microscopes field of view when the wheel-rack stand is placed against the guide with the microscope mounted. A ruler was once again used to ensure that the edge of the metal guide is equidistant from the edge of the plate along its entire length. The metal guide was then secured to the plate using metal clamps. With the metal guide in place, the wheel-rack stand with the

microscope mounted was placed on the surface of the plate such that the rollers were in contact with the edge of the metal guide as depicted in Figure 25.

A.   B.
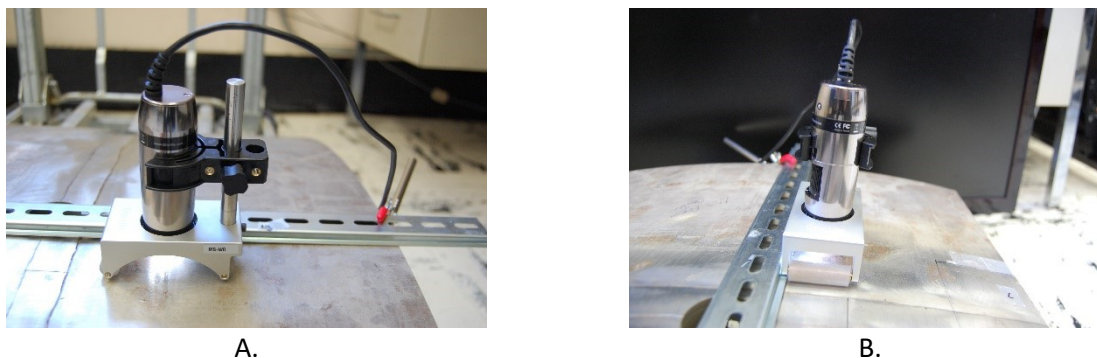
Figure 25: A. The Dino-Lite microscope mounted on the wheel-rack stand with the metal guide mounted to the plate B. the placement of the wheel rack stand against the metal guide

With the microscope set to 50X magnification it was positioned such that the corner of the region of interest was on the edge of the frame and a micrograph was taken. After each micrograph was taken, a landmark is chosen at the inner edge of the microscope field of view and the wheel-rack stand is moved along the guide until the landmark has traversed the entire field of view and is on the opposite edge. The procedure is repeated until the entire width of the region of interest has been micrographed, at which point the clamps securing the metal guide were removed and the metal guide was moved 6.5mm ± 0.5mm further up the plate and resecured before another series of images was taken. This process was repeated until the entire region of interest had been covered. It should be noted that the equipment used for this analysis lacked control in the vertical axis preventing analysis of pit depth in this report. However, this could be rectified by incorporating equipment with vertical control of the microscope, thereby allowing analysis of pit depth in the field as well.

4.2.   Surface Corrosion Coverage

An approximation of the surface area affected by corrosion was determined by superimposing a regular grid over the photo of the plate collected using the Nikon D40 camera. Any cells in the grid where less than half of the surface area of the cell was occupied by the plate were excluded from analysis. With the unoccupied cells removed the remaining cells were examined for visual indicators of corrosion such as surface discoloration, buildup of corrosion products on the surface, or the appearance of corrosion pits on the surface. Figure 26 provides a visualization of this analysis.
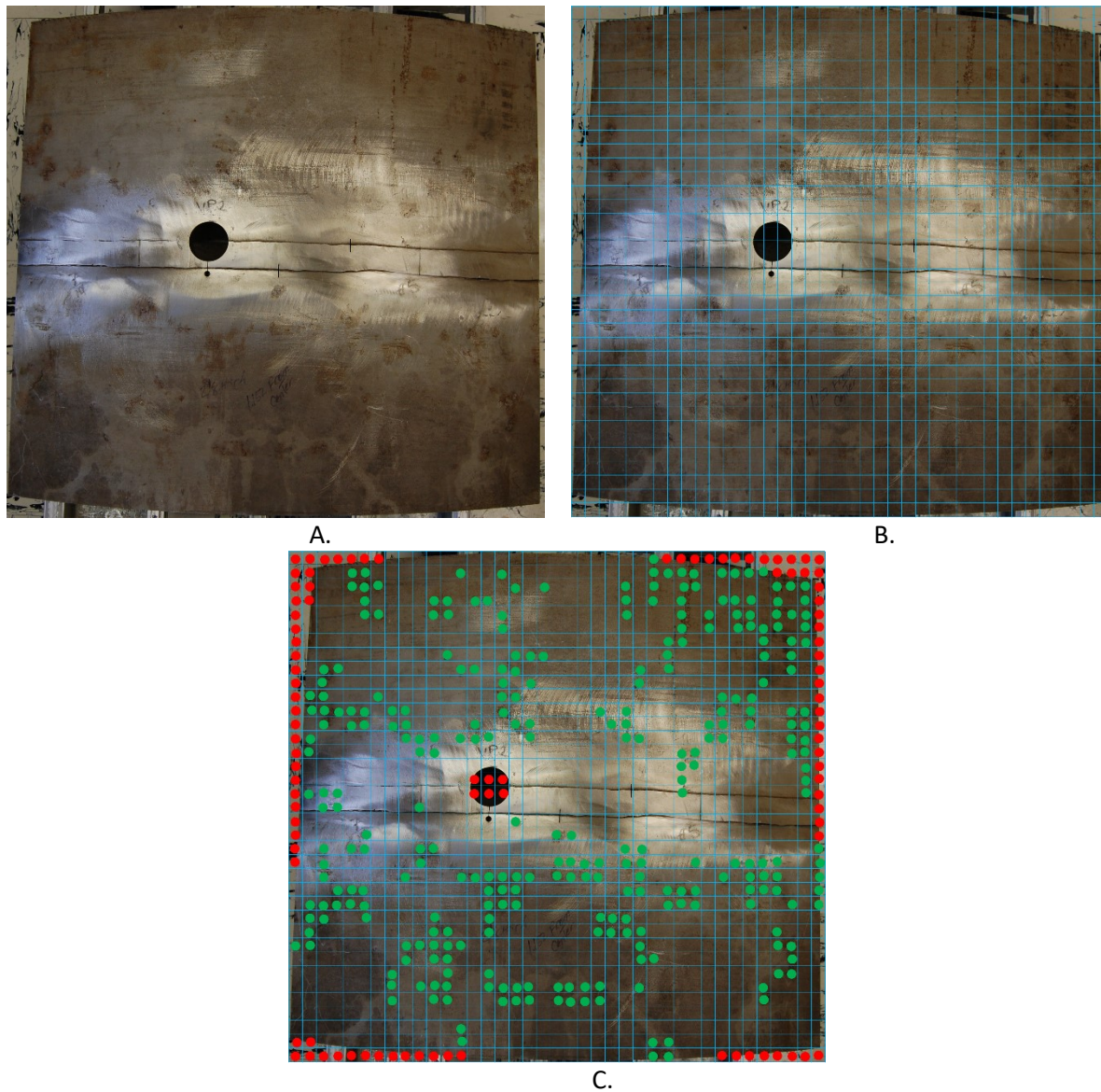
Figure 26: A. Image of plate from Nikon D-40. B. Image of plate with superimposed grid. C. Grid counting analysis of the plate. Red dots correspond to cells that are disregarded, green dots are cells showing visible signs of corrosion.

Visual analysis of the extent of corrosion by grid counting found that 293 out of 1348 cells (see Figure 26 c.) displayed indicators of corrosion equating to approximately 22% of the plate surface. One interesting observation stemming from this analysis is that several areas which appeared corroded in Figure 22 do not have any signs of corrosion left after cleaning. It is worth noting that this analysis is dependent on the indicators of corrosion within a cell being visible in the image. Additionally, the plate exhibits some surface staining that may not be due to corrosion. While efforts were made to distinguish non-corrosion related staining from corrosion

related staining it is still possible that some staining was not properly counted. Due to these factors the estimate for extent of surface corrosion coverage should be considered low accuracy.

Beyond the presence of corrosion on the surface, the preliminary visual analysis also reveals critical details about the character of the plate surface. Specifically, the plate can be broken down into three distinct surface types as depicted in Figure 27.
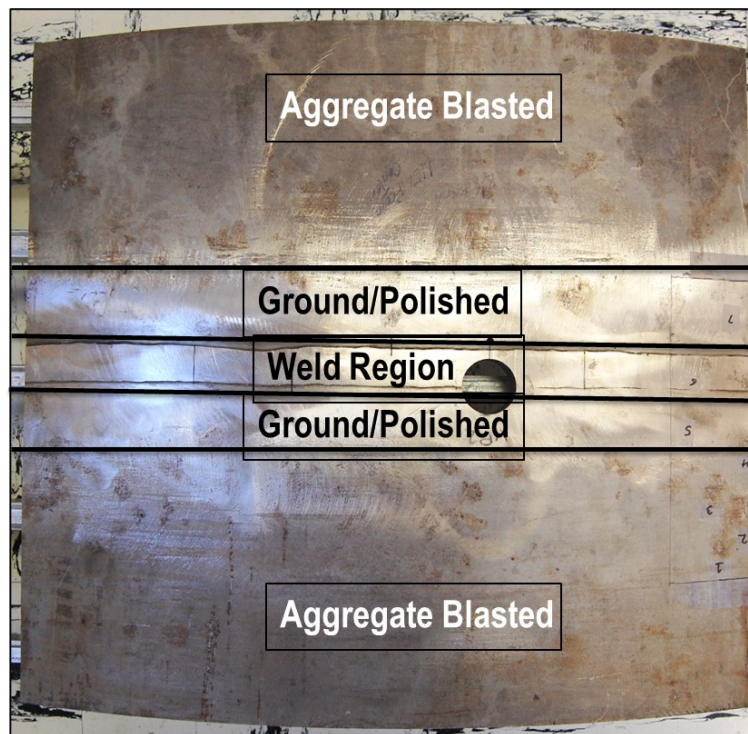
Figure 27: Breakdown of the unique surface types identified by visual analysis

The surface type that makes up the bulk of the plate has a light texturing typical of metals that have undergone some form of aggregate blasting. The next most prolific surface type is seen in the region immediately surrounding the weld line in the center of the plate. This region is characterized by tool markings consistent with grinding or sanding operations performed to flatten and smooth the weld line. Finally, there is the weld line itself which shares the characteristics of the ground region surrounding it but should still be considered separately due to the unique solidification conditions associated with forming a weld.

4.3.   Surface Pitting Analysis

Analysis of corrosion pitting by optical microscopy was performed within a limited region of the plate surface that includes each surface type identified and the transition zones between those surface types. Within this region, seven areas of interest have been identified which show signs of corrosion. These regions were selected because they represent examples of corrosion

occurring in all the distinct regions of the plate surface. The region of interest and the seven areas of interest are depicted in Figure 28.

Figure 28: Region of interest delimited by the metal guide on top, the plate edge on bottom and tape on the left and right. Numbers on tape have been placed on the plate to indicate the seven areas of interest identified for analysis.

Surface corrosion pitting was characterized in a manner as described in section 7.2 of ASTM G46. Since the capability to measure corrosion pit depth is currently not available analysis of corrosion pitting has been limited to density of pits and the cross-sectional areas of the ten largest pits in each area of interest. To acquire the pit density, a 4x4mm box was superimposed over the images with side lengths calibrated based on the scale bar burned onto the images by the microscope. The number of pits contained within the box were counted manually. Specific measurements for the ten largest pits present in each area of interest were also taken by treating the pits as approximate ellipses and superimposing lines over the major and minor axis of the pit which are then used to approximate the area of the pit. The calculation for cross sectional surface area of the pits is:

$$a = \pi * \frac{d_1}{2} * \frac{d_2}{2}$$

Where a is the cross sectional surface area, d_1 is the major axis length, and d_2 is the minor axis length. Figure 29 depicts the process used for pit counting and approximation of cross-sectional area.

a.   b.
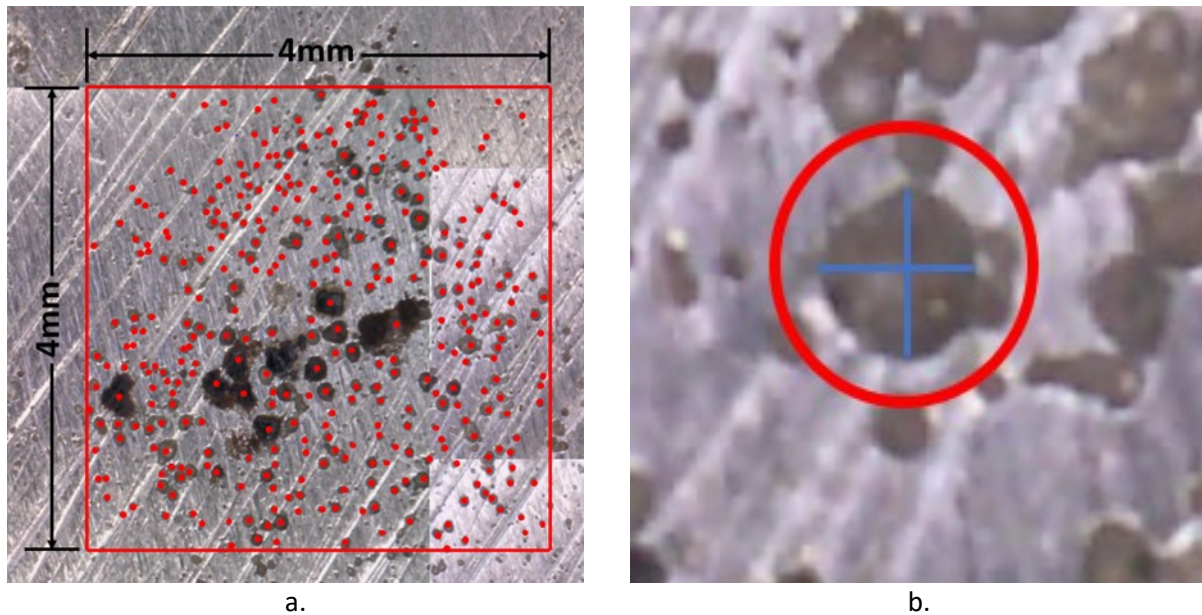
Figure 29: A. Pit counting within a region of interest. Red dots correspond to identified pits, the red square denotes the counting region. B. Measuring approximate major and minor axis (depicted as blue lines). Red circle highlights the pit in question

4.3.1. Pit Density

Analysis of pit density was performed in each of the areas of interest detailed in Figure 28. In keeping with worst case analysis of corrosion behavior the counting regions were selected to reflect the maximum pit density in each area. Composite micrographs of each area of interest with the selected counting regions highlighted are shown in Figure 30.

a.   b.

c.

d.

e.

f.

g.
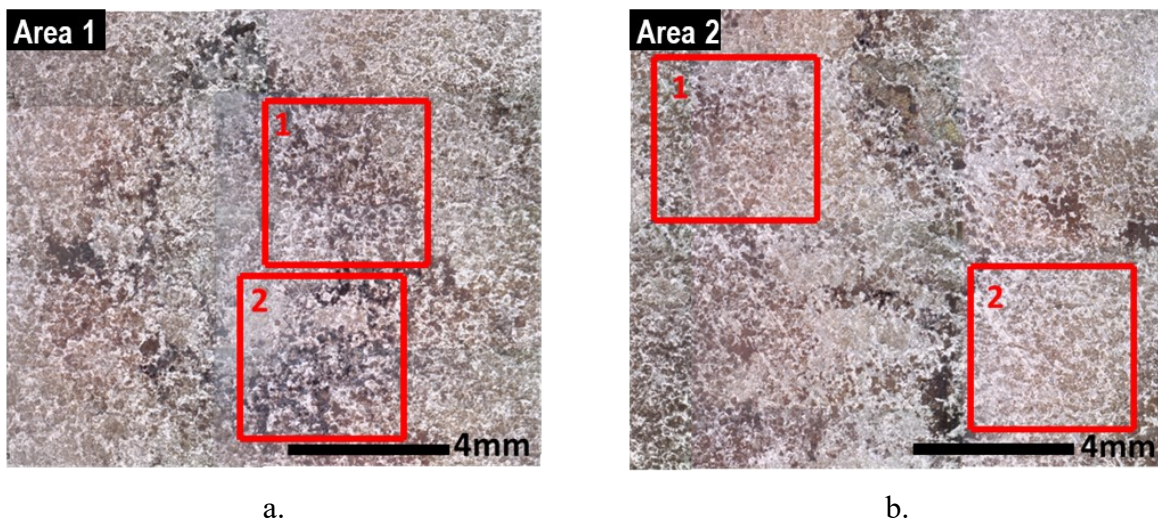
Figure 30: Pit density analysis selections for A. area of interest 4 B. area of interest 6 and C. area of interest 7. The red box denotes the area where counting was performed. Two

regions were selected in region in area of interest 7 since they both appeared as discrete clusters

Results of pit counting analysis are provided in Table 6. The results of pit counting analysis show that pit densities range from 1.19×10^6 pits/m^2 at the low end to 3.87×10^7 pits/m^2 on the high end. The broad range of pit densities can partially be attributed to the differences in the surface texture and material outlined in Figure 4. For example, area of interest 6, which is on the weldment, has a relatively low pit density at 3.25×10^6 pits/m^2 while areas of interest 5 and 7, which are in the ground/polished region, have a high pit density at 2.44×10^7-3.87×10^7 pits/m^2 and 2.28×10^7-2.94×10^7 pits/m^2 respectively. Area of interest 4, which is at the transition between the ground/polished region and the bead blasted region, also has a relatively high pit density at 1.74×10^7 pits/m^2. The areas of interest 1-3 are in the bead blasted region and show the lowest pit densities ranging from a low of 1.19×10^6 to a high of 9.63×10^6. It is important to note that areas of interest 1-3 retained significant quantities of corrosion product after cleaning which could confound pit counting analysis by obscuring or covering pits.

Table 6: Pit density results

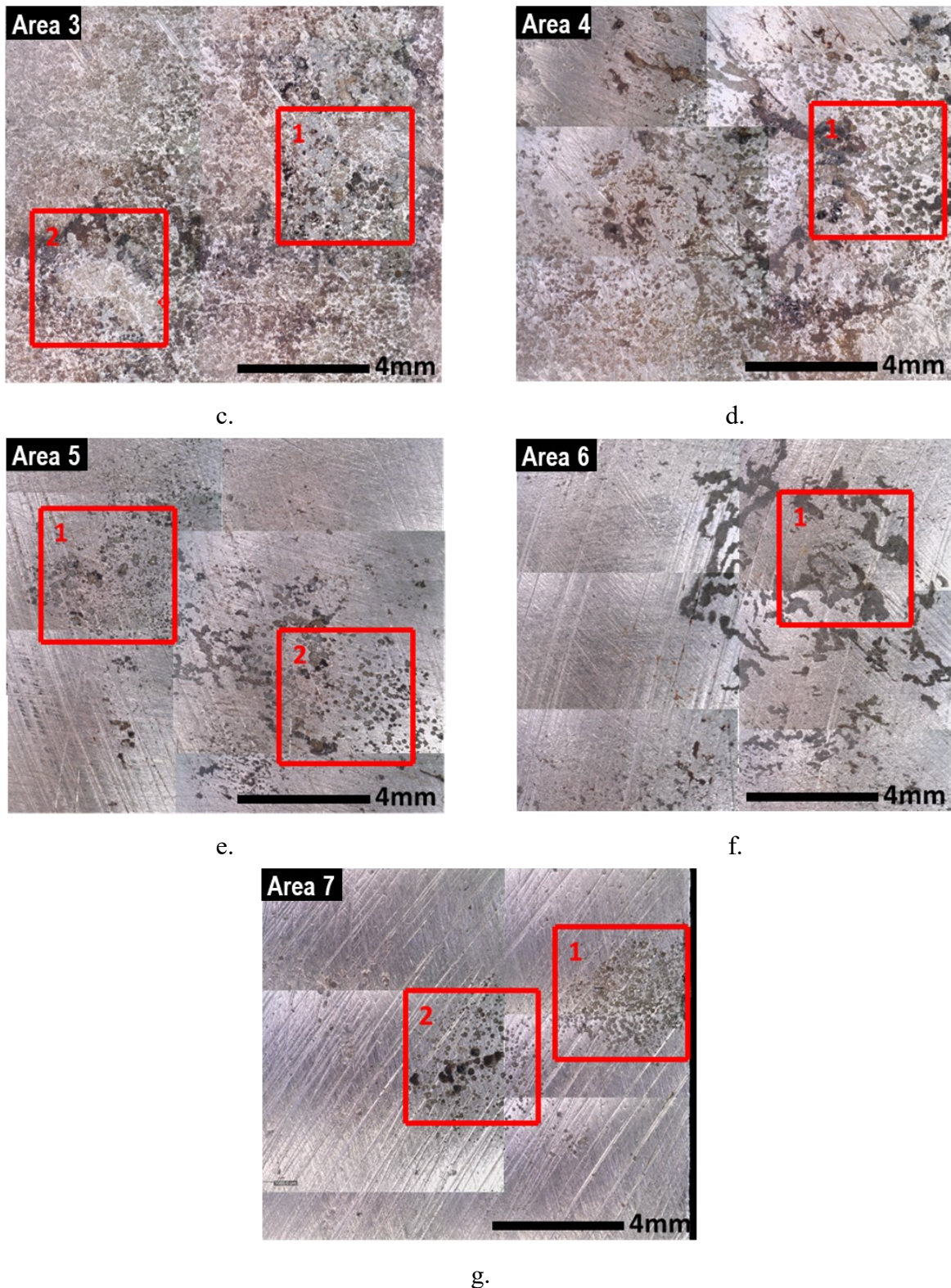| Area of interest	Pit density (pits/m^2)
1.1	2.69×10^6
1.2	3.25×10^6
2.1	1.19×10^6
2.2	2.69×10^6
3.1	9.63×10^6
3.2	4.44×10^6
3.3	4.44×10^6
4	1.74×10^7
5.1	3.87×10^7
5.2	2.44×10^7
6	3.25×10^6
7.1	2.94×10^7
7.2	2.28×10^7

4.3.2. Pit Size

In conjunction with pit counting, analysis of the maximum pit size for areas of interest was also performed. This sort of analysis is consistent with corrosion analysis practices that focus on the most severe examples of pitting identified on a surface to establish an upper bound on corrosion rate. Ten of the largest identifiable pits from each area of interest were selected and analyzed for cross sectional area. While size was the primary factor in pit selection, consideration was also given to select the largest pits which had easily identifiable edges and did not appear to overlap with adjacent pits. The ten largest pit sizes for each area of interest are provided in Table 7.

Table 7: Cross section surface areas (mm²) for the ten largest pits for each area of interest

Pit number	Area 1 (Aggregate)	Area 2 (Aggregate)	Area 3 (Aggregate)	Area 4 (Aggregate)	Area 5 (Aggregate)	Area 6 (Aggregate)	Area 7 (Aggregate)
1	0.0220	0.0158	0.0340	0.0784	0.0368	0.0484	0.0768
2	0.0236	0.0149	0.0227	0.0465	0.0286	0.0186	0.0379
3	0.0342	0.0189	0.0321	0.0377	0.0360	0.0142	0.0329
4	0.0265	0.0285	0.0265	0.0694	0.0314	0.0319	0.0210
5	0.0188	0.0340	0.0198	0.0574	0.0346	0.0334	0.0479
6	0.0123	0.0077	0.0199	0.0569	0.0261	0.0186	0.0235
7	0.0185	0.0143	0.0223	0.0380	0.0311	0.0274	0.0222
8	0.0116	0.0111	0.0377	0.0543	0.0294	0.0197	0.0261
9	0.0177	0.0309	0.0558	0.0401	0.0362	0.0219	0.0274
10	0.0211	0.0171	0.0447	0.0385	0.0304	0.0556	0.0235
Average	0.0206	0.0193	0.0315	0.0517	0.0321	0.0290	0.0339
Maximum	0.0342	0.0340	0.0558	0.0784	0.0368	0.0556	0.0768

The results in Table 7 show that on average the largest pits are present in areas of interest 4 and 7 with the smallest on average present in areas of interest 1 and 2. This may indicate that the dimpled surface texture is less conducive to pit growth than the scratched surface. However, like with the pit density measurements, it is possible that the residual corrosion product present in areas 1 and 2 are obscuring larger pits. Similarly, the largest maximum pit sizes were found in areas of interest 4 and 7 while the smallest maximum pit sizes were once again found in areas of interest 1 and 2. One interesting observation is that corrosion in areas of interest 1-5 and 7 occurs primarily via pitting with oblong pits likely formed of several overlapping pits, while corrosion in area of interest 6 appears to be more inclined toward crevicing or even filiform in nature. The filiform like behavior in the weldment is curious since filiform corrosion is typically associated with lacquered steel and the weld line was not lacquered. It is possible that this was the result of a significant oxide scale forming on the surface of the weldment however, additional examination will be necessary to identify the cause of this difference in behavior.

4.3.3. Examination for Surface SCC

Since images were taken across the entire region of interest, it was possible to perform an analysis of potential for surface SCC formation. The conditions for this analysis were not ideal since the surface of the plate was highly textured by either scratches in the ground/sanded region and weldment region or dimples in the aggregated blasted region. Both surface textures can act to confound attempts to identify cracks by either giving the appearance of a crack that is not present or by obscuring cracks that are present. Having considered these confounding factors, no cracks have been definitively identified within the region of interest.

5. CONCLUDING REMARKS

Tests and experiments were performed on material harvested from the SNL full sized mockup canister to investigate CISCC crack growth behavior in SNF canister materials at exposure conditions whereby sea salt can deliquesce and create a brine electrolyte film at ambient outside temperatures.

Crack Growth Rate (CGR) tests were performed using bolt-load CT (ASTM E1681) and teardrop coupons exposed to sea salt (ASTM D1141) brine environments to interrogate stress intensity factors critical to the onset of CISCC.

All test results from bolt-load CT experiments discussed in this report are consistent with existing experimental data detailed in previous studies [16] [17] [18]. Analysis of the data in this report and the previous studies indicates that all CGR data can be represented by a straight-regression line in semi-logarithmic scale. Based on this analysis, it appears that this simple form of crack growth rate could support the development of ASME BPV Section XI Code Case N-860 in the application of a crack growth rate after a CISCC flaw has been detected by in-service inspection.

A "large plate" experiment was performed using 51x46cm plate harvested from a section of the full sized mockup canister containing a circumferential weld. Several starter cracks were manufactured on the plate and the plate was exposed to a chloride rich environment for two years to simulate CISCC on a canister in a coastal zone. A summary of the experiments performed, and their results is provided in this report.

The experimental design of the "large plate" demonstration incorporated starter defects machined into the outside surface of the plate to act as sites for SCC formation. However, both non-destructive and destructive metallographic examination of the machined defects found that SCC at the machined defects was very minimal. The maximum crack length observed was 44 μm, corresponding to a crack growth rate of 22 μm/year which is less than the lower 95% confidence bound of the literature data as compiled and modeled by SNL for the test temperature (22°C). This model is also used in the ASME N-860 code case.

Analysis of the large plate using techniques applicable to in service inspection of spent nuclear fuel canisters. Analysis using JIS G 0595, as recommended in ASME Section XI Code Case N-860, found a rating between RN-2 (47%) and RN-3 (32%). This rating would fall into the "major" corrosion category defined ASME Section XI Code Case N-860. Despite this rating no major stress corrosion cracking was observed on the plate. Therefore, a set of alternative examination techniques were applied. The first technique utilized grid counting applied over an image of the cleaned plate to gauge the extent of surface corrosion coverage. This analysis found that 22% of the surface showed some sign of corrosion. The second technique utilized a portable, digital microscope mounted on a wheel rack stand to take micrographs of a region of interest and analyze corrosion pitting behavior in a manner like that described in ASTM G46. Analysis using this technique found a maximum pit density of $3.87 x 10^7 \frac{pits}{m^2}$ and a maximum pit size of .0784

mm^2. Micrographic analysis also revealed that corrosion pitting behavior varied depending on surface texture. Pitted surfaces covering most of the plate had low corrosion pit density and small pits, however, these regions also retained corrosion product which possibly obscure some corrosion pitting. The ground/sanded areas surrounding the weld displayed high corrosion pit densities and possessed the largest individual pits. Finally, the weld itself had a relatively low pit density with most of the corrosion occurring by crevicing (possibly filiform). Attempts to identify surface SCC were confounded by the surface texture of the plate. While difficult to detect given the surface finish of the canister plate, no cracks were observed by microscopic examination of the plate surface.

References

[1]   P. S. Lam, A. J. Duncan, L. N. Ward, R. L. Sindelar, Y. J. Kim, J. Y. Jeong, H. J. Lee and M. W. Lee, "Crack Growth Rate Testing and Large Plate Demonstration under Chloride-Induced Stress Corrosion Cracking Conditions in Stainless Steel Canisters for Storage of Spent Nuclear Fuel," *Paper Number PVP2019-94031 in Proceedings of the ASME Pressure Vessels & Piping Conference*, San Antonio, Texas, USA, 2019.

[2]   P. S. Lam, A. J. Duncan and R. L. Sindelar, "Large Plate Experiment of Chloride-induced Stress Corrosion Cracking in Spent Nuclear Fuel Storage Canisters, SRNL-STI-2020-00315," Savannah River National Laboratories, Aiken, South Carolina, USA, 2020.

[3]   A. J. Duncan, L. N. Ward, E. E. Perez, T. T. Truong and R. L. Sindelar, "Large Plate Experiment of Chloride-Induced Stress Corrosion Cracking in Spent Nuclear Fuel Storage Canisters, SRNL-STI-2021-00412," Savannah River National Laboratory, Aiken, South Carolina, USA, 2021.

[4]   P. S. Lam and Y. J. Kim, "I-NERI Project Number 2016-001-K: Flaw Stability and Stress Corrosion Cracking of Austenitic Stainless Steel Canisters for Long Term Storage and Transportation of LWR Used Fuel," U.S. Department of Energy - Office of Nuclear Energy, Washington, D.C., USA, 2016.

[5]   P. E. Zapp, J. M. Duffey, P. S. Lam, K. A. Dunn, D. K. Veirs, L. A. Worl and J. M. Berg, "Relative Humidity and the Susceptibility of Austenitic Stainless Steel to Stress Corrosion Cracking in an Impure Plutonium Oxide Environment," *Journal of Nuclear Materials Management,* vol. 38, no. 3, pp. 4-14, 2010.

[6]   J. I. Mickalonis and J. M. Duffey, "SRNL Shelf Life Studies - SCC Studies at Room Temperature, SRNL-STI-2014-00418," Savannah River National Laboratories, Aiken, South Carolina, USA, 2014.

[7]   A. 5.-1. FFS-1, "Fitness-For-Service (API 579 Second Edition)," American Petroleum Institute, Washington, DC, USA, 2007.

[8]   A. 5.-1. FFS-1, "Fitness-For-Service," American Petroleum Institute, Washington, DC, USA, 2016.

[9]   H. J. Lee, Y. J. Kim, P. S. Lam and R. L. Sindelar, "Engineering J estimates for Spent Fuel Canisters under Combined Mechanical and Welding Residual Stresses," *Paper Number PVP201993936 in Proceedings of the ASME Pressure Vessels & Piping Conference*, San Antonio, Texas, USA, 2019.

[10] A. J. Duncan, P. S. Lam and R. L. Sindelar, "CISCC Experiment of a Large Plate Sectioned from a Spent Nuclear Fuel Canister," *Paper Number PVP2020-21774 in Proceedings of the ASME Pressure Vessels & Piping Conference*, Minneapolis, Minnesota, USA, 2020.

[11] P. S. Lam, P. E. Zapp, J. M. Duffey and K. A. Dunn, "Stress Corrosion Cracking in Tear Drop Specimens," *Paper Number PVP2009-77432 in Proceedings of the ASME Pressure Vessels and Piping DIvision Congerence*, Prague, Czech Republic, 2009.

[12] J. A. Wang, A. Payzant, J. Bunn and K. An, "Neutron Residual Stress mapping for Spent Nuclear Fuel Storage Canister Weldment, ORNL/TM-2018/827," Oak Ridge National Laboratories, Oak Ridge, Tennessee, USA, 2018.

[13] P. S. Lam, "Investigation of the Potential for Caustic Stress Corrosion Cracking of A537 Carbon Steel Nuclear Waste Tanks, SRNS-STI-2009-00564 Rev. 1," Savannah River Nuclear Solutions, Aiken, South Carolina, USA, 2009.

[14] *ASME Boiler and Pressure Vessel Section XI Code Case N-860: "Inspection Requirements and Evaluation Standards for Spent Nuclear Fuel Storage and Transportation Containment Systems",* New York, NY, USA: American Society of Mechanical Engineers.

[15] J. I. Standard, *Rating Method of Rust and Stain of Atmospheric Corrosion for Stainless Steels JIS G 0595: 2004,* Translated to English by Japanese Standards Association, 2005.

[16] A. Ilgen, C. Bryan and E. Hardin, "Draft Geologic Disposal Requirements Basis for STAD Specifications, FCRD-NFST-2013-000723/SAND2015-2175R," Sandia National Laboratories, Albuquerque, New Mexico, USA, 2015.

[17] C. Bryan, R. Dingreville and D. Enos, "Weld Residual Stress Final Results and CISCC Model Development," in *EPRI ESCP Meeting*, Charlotte, North Carolina, USA, 2016.

[18] C. Bryan and D. Enos, "Summary of available data for estimating chloride-induced SCC crack growth rates for 304/316 stainless steel, SAND2016-2992R," Sandia National Laboratories, Albuquerque, New Mexico, USA, 2016.